Cell Reports

Article

Rapid identification of neutralizing antibodies against SARS-CoV-2 variants by mRNA display

Graphical abstract

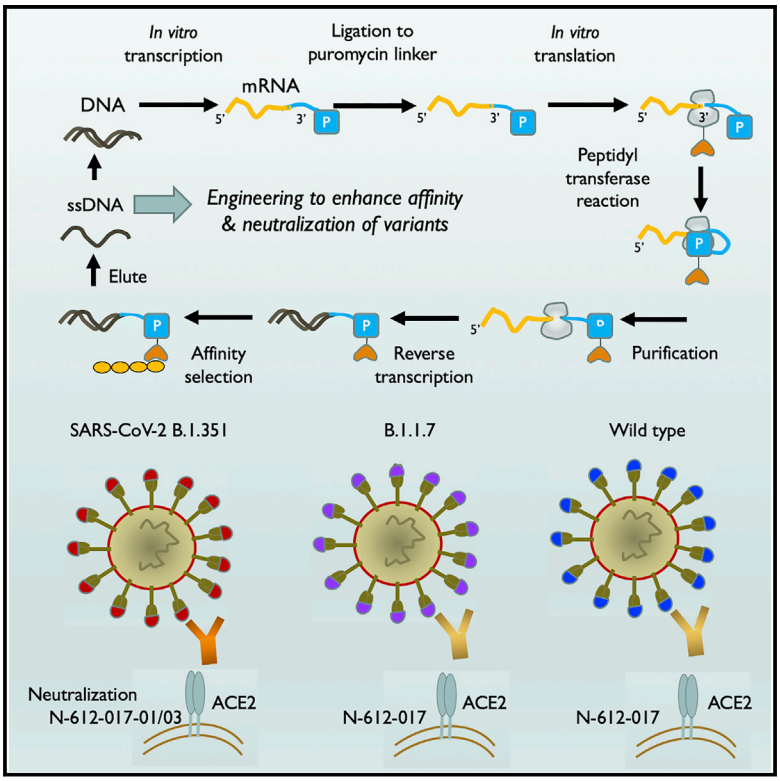

Highlights

- Broadly reactive neutralizing antibodies (nAbs) may overcome SARS-CoV-2 variant escape
- mRNA display is used to rapidly identify SARS-CoV-2 spike (S)-protein-directed nAbs
- Structural studies reveal distinct binding modes for several identified antibodies
- An engineered nAb sustains binding to variant Gamma E484K and Delta L452R spikes

Authors

Shiho Tanaka, C. Anders Olson, Christopher O. Barnes, ..., Kayvan Niazi, Shahrooz Rabizadeh, Patrick Soon-Shiong

Correspondence

patrick@nantworks.com (P.S.-S.), anders.olson@immunitybio.com (C.A.O.)

In brief

Tanaka et al. identify a set of SARS-CoV-2 spike (S)-targeted potentially neutralizing antibodies (nAbs) by mRNA display. Structural analyses reveal distinct binding modes, including the targeting of rare cryptic S receptor-binding domain epitopes. A further engineered ACE2-blocking nAb shows sustained binding to S RBD with the E484K and L452R substitutions.

Tanaka et al., 2022, Cell Reports *38*, 110348
February 8, 2022
https://doi.org/10.1016/j.celrep.2022.110348

CellPress

Cell Reports

CellPress
OPEN ACCESS

Article

Rapid identification of neutralizing antibodies against SARS-CoV-2 variants by mRNA display

Shiho Tanaka,[1,8] C. Anders Olson,[1,8,9,*] Christopher O. Barnes,[2,8] Wendy Higashide,[1] Marcos Gonzalez,[1] Justin Taft,[3,6,7] Ashley Richardson,[3,4,5,6,7] Marta Martin-Fernandez,[3,4,5,6,7] Dusan Bogunovic,[3,4,5,6,7] Priyanthi N.P. Gnanapragasam,[2] Pamela J. Bjorkman,[2] Patricia Spilman,[1] Kayvan Niazi,[1] Shahrooz Rabizadeh,[1] and Patrick Soon-Shiong[1,*]

[1]ImmunityBio, Inc., 9920 Jefferson Boulevard, Culver City, CA 90232, USA
[2]Division of Biology and Biological Engineering, California Institute of Technology, 1200 East California Boulevard, Pasadena, CA 91125, USA
[3]Center for Inborn Errors of Immunity, Icahn School of Medicine at Mount Sinai, 1 Gustave Lane, Levy Plaza, New York, NY 10029-5674, USA
[4]Department of Pediatrics, Icahn School of Medicine at Mount Sinai, 1 Gustave Lane, Levy Plaza, New York, NY 10029-5674, USA
[5]Precision Immunology Institute, Icahn School of Medicine at Mount Sinai, 1 Gustave Lane, Levy Plaza, New York, NY 10029-5674, USA
[6]Mindich Child Health and Development Institute, Icahn School of Medicine at Mount Sinai, 1 Gustave Lane, Levy Plaza, New York, NY 10029-5674, USA
[7]Department of Microbiology, Icahn School of Medicine at Mount Sinai, 1 Gustave Lane, Levy Plaza, New York, NY 10029-5674, USA
[8]These authors contributed equally
[9]Lead contact
*Correspondence: patrick@nantworks.com (P.S.-S.), anders.olson@immunitybio.com (C.A.O.)
https://doi.org/10.1016/j.celrep.2022.110348

SUMMARY

The increasing prevalence of severe acute respiratory syndrome coronavirus 2 (SARS-CoV-2) variants with the ability to escape existing humoral protection conferred by previous infection and/or immunization necessitates the discovery of broadly reactive neutralizing antibodies (nAbs). Utilizing mRNA display, we identify a set of antibodies against SARS-CoV-2 spike (S) proteins and characterize the structures of nAbs that recognize epitopes in the S1 subunit of the S glycoprotein. These structural studies reveal distinct binding modes for several antibodies, including the targeting of rare cryptic epitopes in the receptor-binding domain (RBD) of S that interact with angiotensin-converting enzyme 2 (ACE2) to initiate infection, as well as the S1 subdomain 1. Further, we engineer a potent ACE2-blocking nAb to sustain binding to S RBD with the E484K and L452R substitutions found in multiple SARS-CoV-2 variants. We demonstrate that mRNA display is an approach for the rapid identification of nAbs that can be used in combination to combat emerging SARS-CoV-2 variants.

INTRODUCTION

The emergence of severe acute respiratory syndrome coronavirus 2 (SARS-CoV-2), the causative agent of the respiratory disease coronavirus disease 2019 (COVID-19), has resulted in a pandemic that brought the world to a standstill (Zhou et al., 2020). Despite the rapid development and success of vaccines and antibody therapies, ongoing SARS-CoV-2 antigenic drift has resulted in the emergence of variants that pose new threats (Davies et al., 2021; Plante et al., 2021; Yurkovetskiy et al., 2020). Various studies have shown that several of these variants have the ability to escape antibody neutralization mediated by antisera from recovered COVID-19 patients/vaccinated individuals or recombinant neutralizing antibodies (nAbs) developed as therapeutics (Cerutti et al., 2021; McCallum et al., 2021a; Suryadevara et al., 2021). Thus, along with modified vaccines to combat variants, there is an urgent need for the development of prophylactic and therapeutic anti-viral drugs, including biologics such as nAbs, with sustained efficacy against SARS-CoV-2 variants.

The trimeric SARS-CoV-2 spike (S) glycoprotein serves as the fusion machinery for viral entry and therefore represents the main target of nAbs (Brouwer et al., 2020; Cao et al., 2020; Robbiani et al., 2020). The SARS-CoV-2 S trimer utilizes the angiotensin-converting enzyme 2 (ACE2) as its host receptor (Hoffmann et al., 2020; Li et al., 2003; Zhou et al., 2020) through interactions with the receptor-binding domains (RBDs) located at the apex of the S trimer. The RBDs adopt either ''down'' or ''up'' conformations, with RBD binding to ACE2 facilitated only by the upconformation (Kirchdoerfer et al., 2016; Li et al., 2019; Walls et al., 2016, 2020; Wrapp et al., 2020; Yuan et al., 2017). While the majority of potent anti-SARS-CoV-2 nAbs target the RBD and directly compete with ACE2 binding (Barnes et al., 2020a; Brouwer et al., 2020; Cao et al., 2020; Robbiani et al., 2020), recent studies have revealed nAbs that target the N-terminal domain (NTD) (Liu et al., 2020; McCallum et al., 2021b) and the S2 stem helix (Zhou et al., 2021).

The structures of numerous monoclonal antibodies (mAbs) recognizing the RBD and the NTD have been characterized (Barnes et al., 2020a, 2020b; Baum et al., 2020; Brouwer et al., 2020; Hansen et al., 2020; Pinto et al., 2020), enabling their classification based on shared epitopes and neutralizing properties (Barnes et al., 2020b; Dejnirattisai et al., 2021; McCallum et al.,

2021b; Yuan et al., 2021). A subset of mAbs that recognize non-overlapping epitopes are in clinical trials or have received emergency use authorization from the US Food and Drug Administration (FDA) for the treatment and prevention of COVID-19 (Cathcart et al., 2021; Jones et al., 2021; Weinreich et al., 2021). However, ongoing viral evolution and genetic drift have resulted in an accumulation of mutations and/or deletions found in the S RBD and NTD that enhance the affinity of ACE2 binding and allow some variants to evade existing immunity (Cele et al., 2021; Tegally et al., 2021). Thus, current emergency-authorized therapies developed early in the pandemic based on the first-wave or "A" strain S sequence could potentially be less effective against emerging SARS-CoV-2 variants that harbor escape mutations mapped to their epitopes (Greaney et al., 2021a, 2021b; Starr et al., 2020, 2021; Weisblum et al., 2020).

Here, we report our identification via mRNA display (Newton et al., 2020; Olson et al., 2008; Roberts and Szostak, 1997; Takahashi et al., 2003) of a set of mAbs targeting SARS-CoV-2 S, which we demonstrate neutralize both authentic and pseudoviral SARS-CoV-2 with half-maximal inhibitory concentrations (IC_{50}s) between 0.076 and 7.0 μg/mL. Structural analysis revealed that a subset of these nAbs recognize RBD and NTD epitopes, including a rare, cryptic, cross-reactive RBD epitope. Moreover, we characterize a weak nAb that recognizes the S1 subdomain 1 (SD1), providing insight into a class of antibodies that are infrequently found among convalescent individuals (Zost et al., 2020a; 2020b) that can be utilized in the fight against COVID-19. Finally, we describe the utility of mRNA display for the rapid identification of variant-resistant antibody clones. This powerful technique enabled the rapid selection of a discovered SARS-CoV-2 nAb to extend its neutralizing capability to SARS-CoV-2 expressing the E484K and L452R S RBD mutations found in multiple SARS-CoV-2 variants.

RESULTS

Identification of anti-SARS-CoV-2 S antibodies by mRNA display

We utilized mRNA display of a synthetic, human VH3/Vκ1 single-chain variable fragment (scFv) library (Olson, 2021) to identify mAbs targeting the S protein of SARS-CoV-2. Briefly, after four rounds of selection using the stabilized S trimer, we rapidly identified scFv hits to convert to immunoglobulin G1 (IgG1). The top 10 mAbs chosen for evaluation were found to bind multiple domains on S (Table S1). S comprises an N-terminal fragment known as S1, which further divides into the NTD, the ACE2 RBD, small C-terminal subdomains 1 and 2 (SD1 and SD2), and a C-terminal "S2" fragment (Figure 1A). Bio-layer interferometry (BLI) kinetic analysis using recombinant SARS-CoV-2 RBD (residues 319–541), RBD-SD1 (residues 319–591), S1 (residues 16–685), and S2 (residues 686–1213) proteins revealed that 3 antibodies bind the RBD (N-612-017, N-612-056, and N-612-074), 2 antibodies bind the SD1 domain (N-612-004 and N-612-041), 2 antibodies bind the NTD (N-612-002 and N-612-014), and 3 antibodies bind the S2 domain (N-612-007, N-612-044, and N-612-086) (Figures 1A–1C). All 10 antibodies bind corresponding binding domains with low nM binding affinity (K_D) (Figure 1B; Table S2 supplemental information), but apparent affinities are far superior (K_D < 3 pM) for S trimers (Figures 1B and 1C; Table S3). Among the 3 RBD binders, only N-612-017 showed competition with ACE2 binding (Figure 1D).

To further map the binding regions of the 10 antibodies, we performed epitope binning experiments using S1 and S2 fragments separately (Figure 1E). Two NTD binders blocked each other but not RBD- or SD1-binding antibodies. The 3 RBD binders competed with each other (Figures 1E and 1F) despite N-612-017 being the only ACE2 blocker (Figure 1D). SD1 binders N-612-004 and N-612-041 blocked each other, but only N-612-041 blocked N-612-074 (an RBD binder), suggesting that N-612-041 and N-612-074 have proximal or overlapping binding sites (Figures 1E and 1F). Epitope binning using the S2 domain revealed that N-612-007 and N-612-044 are non-competing, whereas N-612-086 competes with both N-612-007 and N-612-044, suggesting that they all bind distinct epitopes on S2 (Figures 1E and 1F).

In addition, multiple biophysical assays were carried out to determine the developability of all 10 antibodies (Table S4) (Jain et al., 2017). All 10 mAbs displayed low polyreactivity scores by meso scale diagnostic (MSD) analysis and low self-interaction scores by BLI-clone self-interaction (CSI) (Table S4). Eight of the mAb candidates exhibited low hydrophobicity in the hydrophobic interaction column (HIC) chromatography, while higher hydrophobicity was observed for N-612-041 and N-612-074 (Table S4). N-612-041 also showed more rapid aggregation in an accelerated stability assay system, while the other 9 mAbs demonstrated long-term stability (Table S4). Furthermore, all 10 mAbs exhibited desirable thermostability of Fab in differential scanning fluorimetry (DSF) melting temperature (Tm) analysis (Ionescu et al., 2008) (Table S4; Figure S1), although N-612-044 exhibited heterogeneous characteristics in thermostability and HIC chromatography. Ultimately, 7 out of the 10 antibodies displayed biophysical characteristics within the acceptance criteria, indicating that antibodies engineered by mRNA display can have favorable developability.

Neutralization activity assessment of anti-SARS-CoV-2 antibodies

Ten mAbs identified by mRNA display were assessed for neutralization activity against authentic SARS-CoV-2 virus in a Vero E6 cell neutralization assay. The ACE2-blocking anti-RBD antibody N-612-017 demonstrated the highest neutralization activity, and the non-ACE2-blocking RBD binder N-612-056 showed a weaker but nearly complete neutralization of ~87% (Figure 2A). N-612-004 (SD1 binder), N-612-007 (S2 binder), and N-612-014 (NTD) antibodies all showed some neutralization activity that plateaued at 40%–60% (Figure 2A), similar to previous observations made for anti-NTD antibodies (McCallum et al., 2021b). We next investigated the activity of N-612-017 in combination with N-612-004, N-612-007, and N-612-014. N-612-017 and respective partners were mixed in equal concentrations. All combinations tested showed slightly improved IC_{50} values compared with N-612-017 by itself, suggesting that both antibodies present in mixture can bind to S simultaneously and, in some cases, non-RBD domain binders can enhance the activity of RBD-binding nAbs (Figures 2B–2D).

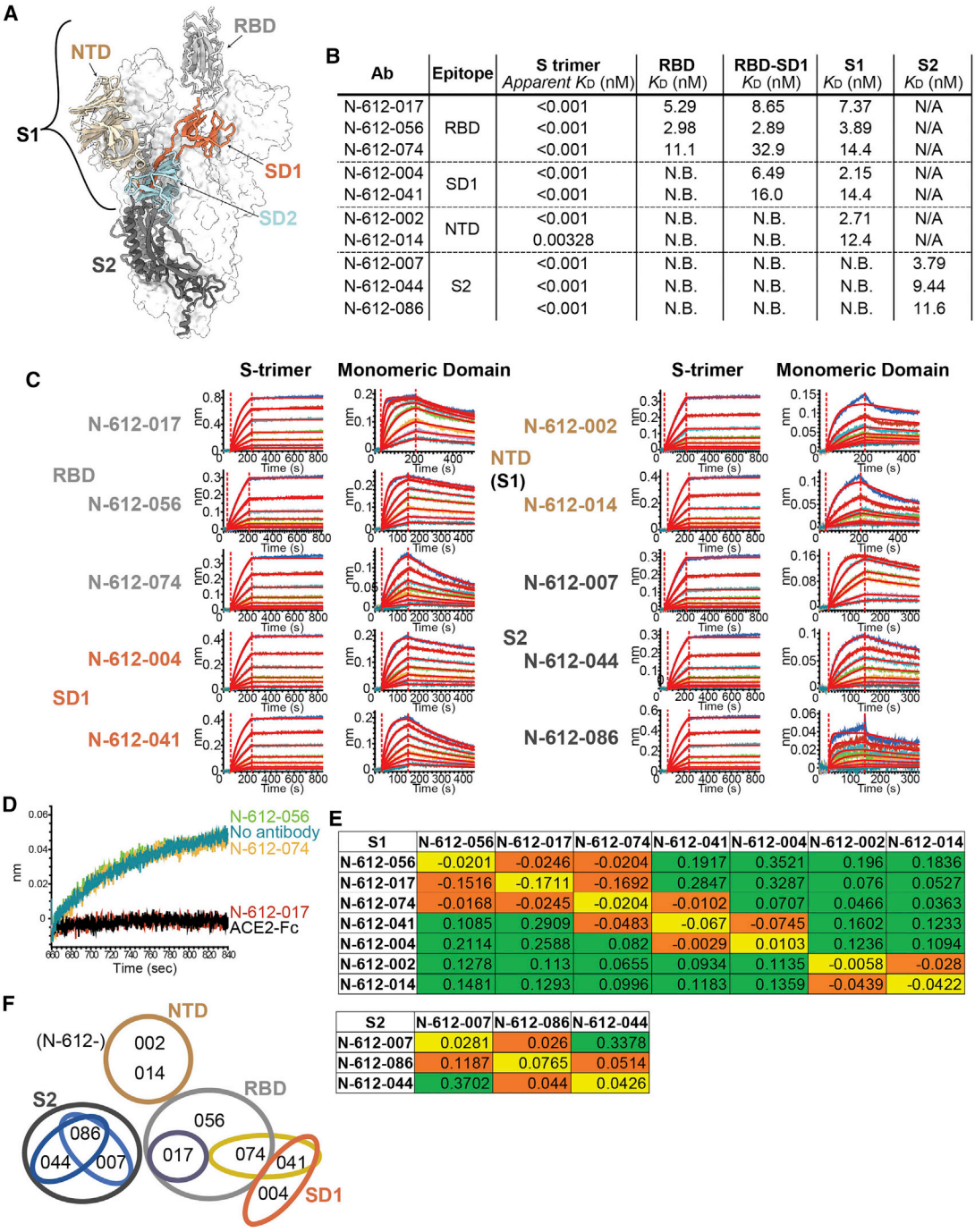

Ab	Epitope	S trimer *Apparent* K_D (nM)	RBD K_D (nM)	RBD-SD1 K_D (nM)	S1 K_D (nM)	S2 K_D (nM)
N-612-017	RBD	<0.001	5.29	8.65	7.37	N/A
N-612-056		<0.001	2.98	2.89	3.89	N/A
N-612-074		<0.001	11.1	32.9	14.4	N/A
N-612-004	SD1	<0.001	N.B.	6.49	2.15	N/A
N-612-041		<0.001	N.B.	16.0	14.4	N/A
N-612-002	NTD	<0.001	N.B.	N.B.	2.71	N/A
N-612-014		0.00328	N.B.	N.B.	12.4	N/A
N-612-007	S2	<0.001	N.B.	N.B.	N.B.	3.79
N-612-044		<0.001	N.B.	N.B.	N.B.	9.44
N-612-086		<0.001	N.B.	N.B.	N.B.	11.6

S1	N-612-056	N-612-017	N-612-074	N-612-041	N-612-004	N-612-002	N-612-014
N-612-056	-0.0201	-0.0246	-0.0204	0.1917	0.3521	0.196	0.1836
N-612-017	-0.1516	-0.1711	-0.1692	0.2847	0.3287	0.076	0.0527
N-612-074	-0.0168	-0.0245	-0.0204	-0.0102	0.0707	0.0466	0.0363
N-612-041	0.1085	0.2909	-0.0483	-0.067	-0.0745	0.1602	0.1233
N-612-004	0.2114	0.2588	0.082	-0.0029	0.0103	0.1236	0.1094
N-612-002	0.1278	0.113	0.0655	0.0934	0.1135	-0.0058	-0.028
N-612-014	0.1481	0.1293	0.0996	0.1183	0.1359	-0.0439	-0.0422

S2	N-612-007	N-612-086	N-612-044
N-612-007	0.0281	0.026	0.3378
N-612-086	0.1187	0.0765	0.0514
N-612-044	0.3702	0.044	0.0426

Figure 1. Identification of SARS-CoV-2 Spike-targeting monoclonal antibodies

(A) Model of the SARS-CoV-2 spike trimer domains (PDB: 6VYB): NTD (wheat), RBD (light gray), SD1 (coral), SD2 (powder blue), and S2 (dark blue).

(B) K_D summary table from BLI kinetic analysis of 10 antibodies against spike trimer and various domains used as analytes. N.B., no binding; N/A, untested. Apparent K_D values for the spike (S) trimer were obtained by curve fitting with a bivalent model, and due to the very slow off rate, apparent K_D values may not be accurate.

(C) BLI kinetic analysis of 10 antibodies against the S trimer (left) and each corresponding domain (right).

(D) BLI blocking assay: biosensors were coated with RBD, and subsequently, all RBD binding antibodies (N-612-017, N-612-056, and N-612-074) and ACE2-IgG1Fc were incubated with RBD-coated biosensor. The recorded signal from ACE2-IgG1Fc binding to the RBD on the biosensor indicates the RBD blocking capability of the test samples. Both N-612-017 and ACE2-IgG1Fc completely blocked RBD and ACE2 interactions.

(E) Epitope binning data indicating competing antibody pairs in red and non-competing antibody pairs in green. Self-blocking is in orange.

(F) Epitope binning diagram mapping overlapping regions of binding sites of 10 mAbs.

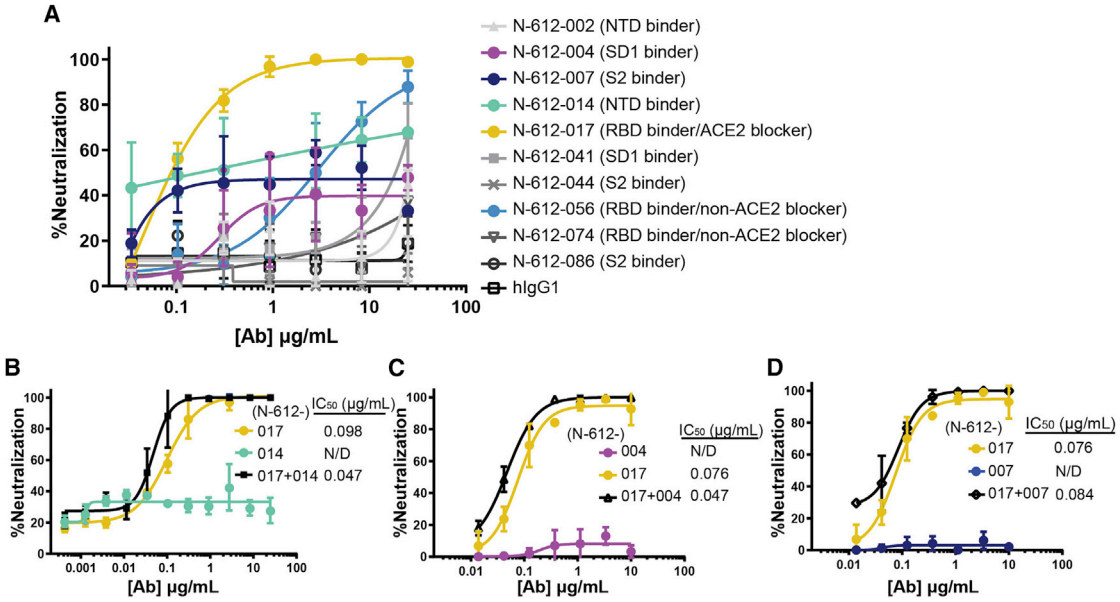

Figure 2. Neutralization activity of mAbs in Vero E6 live virus neutralization assay

(A) Dose-dependent neutralization of SARS-CoV-2 virus by 10 mAbs selected by mRNA library display.

(B–D) N-612-017 neutralization activity in combination with (B) N-612-014, (C) N-612-004, and (D) N-612-007. The X axis represents the concentration of antibodies when used alone; when antibodies were combined, an equal concentration of each antibody was used. Mean and standard deviation of duplicate experiments (n = 3) are shown.

Neutralization activity of N-612-014 (NTD binder) showed variable saturation between assays and prevented accurate IC_{50} determination (Figure S2A). To test whether the activity of N-612-014 changes in a time-dependent manner, we tested the effects of longer antibody-virus incubation times on neutralization potency. With a virus-antibody incubation time of ~30 min, neutralization activity plateaued between 20% and 90% (Figure S2A). In contrast, when the virus was incubated with an antibody for 24 h before the exposure of cells to the complexes, neutralization activity plateaued at ~90% with IC_{50} values of 0.023–0.025 µg/mL (Figure S2B). Longer incubation also resulted in improved neutralization potencies for positive control convalescent serum, N-612-014, N-612-056, and N-612-017 (Figures S2B–S2E), suggesting a change in viral infectivity due to a time-dependent conformational change in S (Huo et al., 2020; Wec et al., 2020) or, possibly, the relatively poor accessibility of the epitopes targeted by these antibodies.

Structural characterization of RBD-specific, ACE2-blocking nAb N-612-017

To investigate the specificity of RBD targeting for nAbs N-612-017 and N-612-056, we determined a 3.2 Å single-particle cryo-electron microscopy (cryo-EM) structure of a complex between SARS-CoV-2 S trimer and the N-612-017 Fab (Figures 3 and S3; Table S5) and a 2.9 Å X-ray crystal structure of a SARS-CoV-2 RBD-N-612-056 Fab complex (Figure 4; Table S6). The N-612-017-S trimer complex structure revealed N-612-017 Fab binding to both up and downRBD conformations and the recognition of an epitope that partially overlapped with the ACE2 receptor-binding site (Figures 3A and 3B), consistent with BLI competition data (Figure 1D). N-612-017 uses five of its six complementarity-determining region (CDR) loops and HC framework region 3 (FWR3) to interact with an epitope focused on RBD residues adjacent to the ACE2 receptor-binding ridge (Figures 3C and 3D), resulting in ~1,018 $Å^2$ buried surface area (BSA) on the epitope. The CDRH2 and CDRH3 loops mediate the majority of RBD contacts (~616$Å^2$ of ~1,030$Å^2$ total paratope BSA), establishing hydrophobic and hydrogen bond interactions at the Fab-RBD interface. Of note, N-612-017 CDRH2 loop residues contact RBD positions frequently mutated among circulating variants (Deng et al., 2021; Kuzmina et al., 2021; McCallum et al., 2021a; Wang et al., 2021). RBD residue $E484_{RBD}$ established hydrogen bond interactions with $G52_{HC}$ and $G54_{HC}$ in CDR2 and $D72_{HC}$ in FWR3 (Figure 3E), while $L452_{RBD}$ formed stacking interactions with CDR2 residue $Y52_{HC}$ (Figure 3F). Taken together, these data indicate nAb N-612-017 targets the RBD similarly to nAbs that belong to the class 2 binding mode, which is the predominant nAb class identified in convalescent and vaccinated donors (Barnes et al., 2020b; Wang et al., 2021).

Structural characterization of RBD-specific nAb N-612-056 targeting cryptic site

Next, we analyzed the high-resolution X-ray crystal structure of the SARS-CoV-2 RBD-N-612-056 Fab complex (Figure 4A). This method was used rather than cryo-EM due to N-612-056's lack of binding to intact S trimers (Figure 4A, inset). Similar to the donor-derived antibody COVOX-45 (Dejnirattisai et al., 2021), N-612-056 binds a rare cryptic epitope that is not readily found in the repertoire of antibodies from convalescent donors (Figure S4). Consistent with observed binding to dissociated

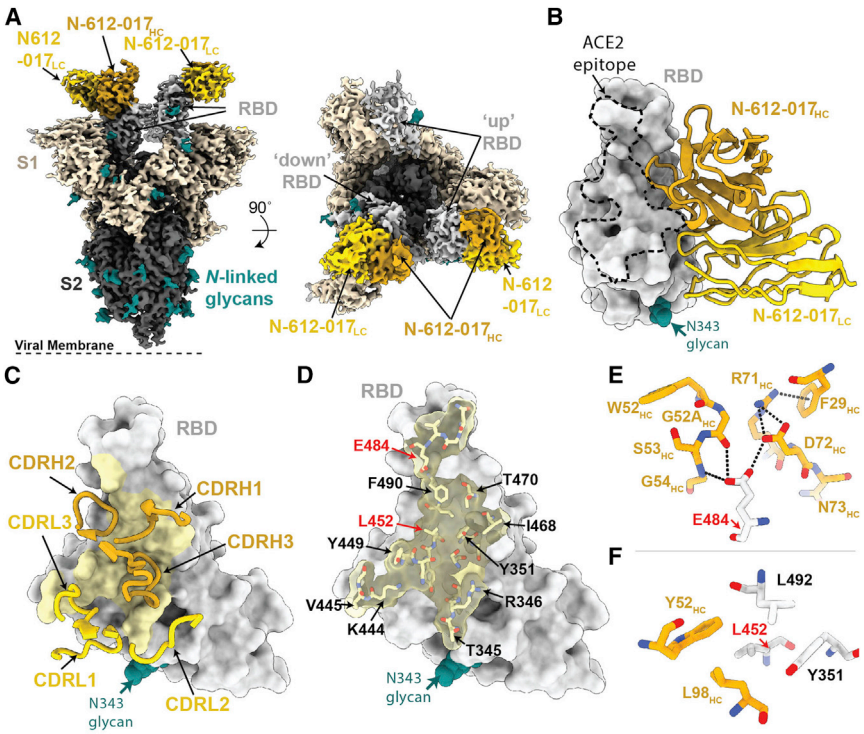

Figure 3. Cryo-EM structure of the N-612-017-S complex

(A) Cryo-EM density for the N-612-017-S trimer complex. Side view (left panel) illustrates the orientation with respect to the viral membrane (dashed line).

(B) Close-up view of N-612-017 variable domains (HC, gold; LC, yellow) bound to RBD (gray surface). The ACE2 receptor-binding site is shown as a dashed line.

(C) N-612-017 CDR loops mapped on the RBD.

(D) Surface and stick representation of N-612-017 epitope (yellow) on RBD surface (gray).

(E and F). Residue-level interactions between N-612-017 (gold) and SARS-CoV-2 RBD (gray). Potential hydrogen bond interactions are illustrated by dashed black lines.

S1 protomers by single-particle cryo-EM (data not shown), the N-612-056 cryptic epitope is inaccessible on an S trimer due to steric clashes with the neighboring NTD and does not overlap with the ACE2 binding site (Figures 4A and 4B). N-612-056 HC and LC CDR loops participate equally to bury ~890 Å^2 of the RBD epitope surface area that comprises residues 352–357 in the β1 strand, which is part of a structurally conserved 5-stranded RBD β-sheet, and residues 457–471 that comprise a disordered loop directly beneath the ACE2 receptor-binding ridge (Figures 4C and 4D).

N-612-056 establishes a network of hydrogen bond and hydrophobic interactions that include a stretch of hydrophobic residues in CDRH3 that mediate van der Waals interactions at the RBD interface and the formation of salt bridges between N-612-056 residues D28$_{LC}$ and E55$_{LC}$ with R346$_{RBD}$ and R357$_{RBD}$, respectively (Figure 4E). These structural data explain the observed cross-reactivity against SARS-CoV RBD (Figure S5A) (Cohen et al., 2021), as 14 of the 20 epitope residues are strictly conserved, and three additional residues (R346, R357, and K462 SARS-CoV-2 RBD numbering) are conservatively substituted (K333, K344, and R449 SARS-CoV RBD numbering) in SARS-CoV and SARS-CoV-2 (Figure 4F). Overall, these structural data for the two RBD-targeting nAbs analyzed suggest comparable modes of recognition and neutralization for antibodies N-612-017 and N-612-056, which were selected from mRNA display, as those identified in convalescent or vaccinated donors.

Structural characterization of S1-specific antibodies N-612-014 and N-612-004

The primary target of SARS-CoV-2 nAbs is the viral S glycoprotein, with the majority of nAbs targeting the RBD (Greaney et al., 2021a; Piccoli et al., 2020). The S NTD represents a common site of antigenic drift (Cele et al., 2021; McCarthy et al., 2021; Ribes et al., 2021), and nAbs that bind to this region have recently been identified (Cerutti et al., 2021; McCallum et al., 2021b; Suryadevara et al., 2021). To understand the binding mode of the NTD-targeting antibody N-612-014 (Figure 1), we determined a 3.5 Å cryo-EM structure of N-612-014 Fabs complexed with stabilized S trimers (Figures 5A and S3). N-612-014 adopted a binding pose parallel to the viral membrane and primarily used HC CDR loops to recognize an epitope at the periphery of the NTD (Figures 5A–5C). The NTD epitope recognized by N-612-014 closely resembles that recognized by the human-derived SARS-CoV-2 antibody S2X316 that targets NTD antigenic site v, which resides outside of the antigenic supersite (site i), the main target of neutralizing NTD antibodies (McCallum et al., 2021b). The N-612-014 epitope (~1,070 Å^2 epitope BSA) involves contacts with peripheral loops comprising NTD residues 68–78, 175–188, and 245–260, as well as contacts with the tip of the supersite β-hairpin (Figures 5D and 5E). Despite contacts with residues 69-70$_{NTD}$ and 144$_{NTD}$, N-612-014 maintains binding to S trimers of the B.1.1.7 lineage sequence (Figure S5), which has deletions at these positions that allow escape from NTD supersite antibodies (McCallum et al., 2021b). These data suggest that N-612-014 retains NTD binding capability and may retain potency in the presence of NTD mutations commonly found in viral variants.

In addition to N-612-014, we also identified antibody N-612-004, an S1-specific antibody that was mapped to a domain outside of the NTD and RBD (Figure 1). Using single-particle cryo-EM, we determined that a 4.8 Å structure of N-612-004 bound to a dissociated S1 protomer, which revealed recognition of an SD1 epitope (Figures 5F and S3). Consistent with our library design that varied CDR loops H2, H3, and L3, N-612-004 contacts were solely mediated by these three regions, which led to the recognition of loops 556–563 and 567–569 in the SD1 domain (Figure 5G). The epitope for N-612-004 is not accessible

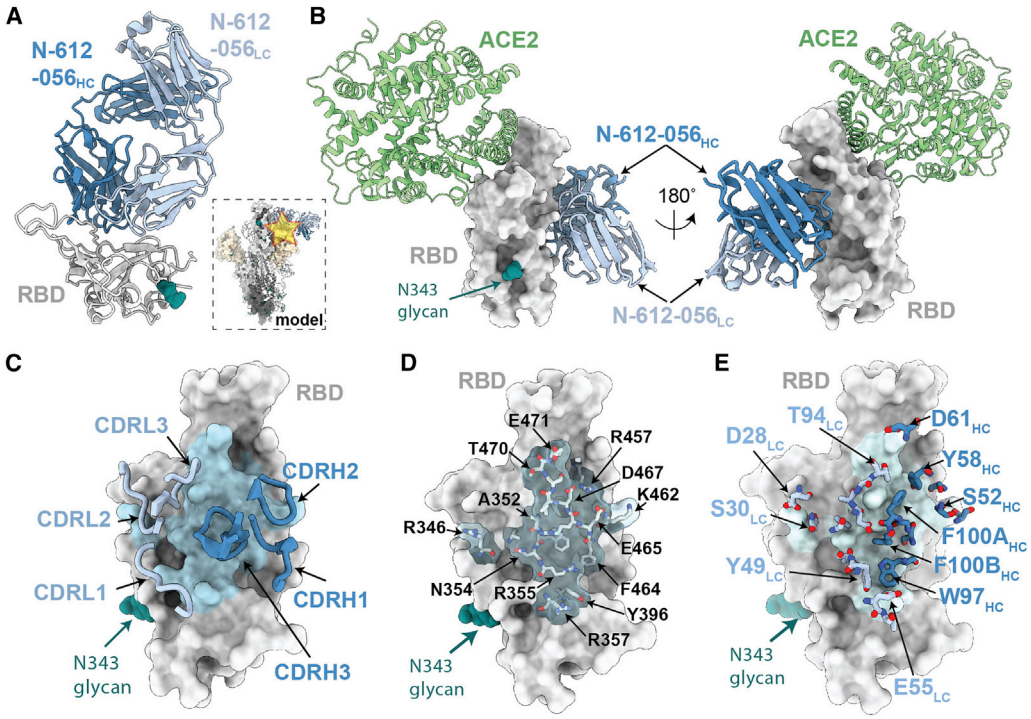

F

```
                331       340       350       360       370       380       390       400       410       420
                |         |         |         |         |         |         |         |         |         |
SARS-CoV-2      NITNLCPFGEVFNATRFASVYAWERKRISNCVADYSVLYNSASFSTFKCYGVSPTKLNDLCFTNVYADSFVIRGDEVRQIAPGQTGKIADYNYK
SARS-CoV        ...............K.P........K..............TF..........A........S.........VK..D..........V.......
WIV1-CoV        ...............T.P........................T..........A........S.........VK..D..........V.......
SCH014-CoV      ...............T.P........................T..........A........S.........VK..D..........V.......
S309 epitope      ### # ### ####        # ######

                430       440       450       460       470       480       490       500       510
                |         |         |         |         |         |         |         |         |
SARS-CoV2       LPDDFTGCVIAWNSNNLDSKVGGNYNYLYRLFRKSNLKPFERDISTEIYQAGSTPCNGVEGFNCYFPLQSYGFQPTNGVGYQPYRVVVLSFELL
SARS-CoV        .....M...L...TR.I.ATST.....K..YL.HGK.R.......NVPFSPDGK..TP-PAL...W..ND...YT.T.I..............
WIV1-CoV        .........L...SR.I.ATQT.....K..SL.HGK.R.......NVPFSPDGK..TP-PA....W..ND...YI...I..............
SCH014-CoV      .....L...L...T.SK..STS........WV.R.K.N.Y...L.ND..SP.GQS.SA-V.P...N..RP...FT.A...H.............
S309 epitope                ##  #
```

Figure 4. X-ray crystal structure of SARS-CoV-2 RBD in complex with the N-612-056 Fab

(A) 2.9 Å X-ray crystal structure for the N-612-056 Fab-RBD complex. Inset: overlay of the N-612-056-RBD crystal structure on an S trimer with up RBD conformation (PDB: 6VYB).

(B) Composite model of N-612-056-RBD (blue ribbon and gray surface, respectively) overlaid with soluble ACE2 (green; PDB: 6M0J). The model was generated by aligning RBDs on 191 matched Cα atoms.

(C) N-612-056 CDR loops (blue) mapped on the RBD surface (gray). The N-612-056 epitope is shown as a light blue surface.

(D) Surface and stick representations of N-612-056 epitope.

(E) N-612-056 paratope residues mapped on the RBD surface with epitope residues shown in light blue.

(F) Sequence alignment of SARS-CoV-2, SARS-CoV, WIV1-CoV, and SCH014-CoV. N-612-056 epitope residues are shaded blue. S309 epitope residues are also shown (indicated with the hash [#] symbol).

on S trimers, which likely explains the lack of N-612-004-like antibodies identified among a repertoire of antibodies found in convalescent plasma (Figure S4).

Activity of identified nAbs against variants

To assess the relative affinity of RBD-binding nAbs N-612-017 and N-612-056 against a series of variants, BLI was performed using RBD variants B.1.1.7 (N501Y), B.1.351 (K417N/E484K/N501Y), CAL.20C (L452R), and A.VOI.V2 (T478R/E484K) with single or combined mutations. N-612-056 binding affinity was not affected by any of the RBD mutations tested, which was anticipated based on structural characterization findings that indicate N-612-056 recognizes a more conserved epitope on the surface of RBD. Neither N501Y (the only RBD mutation in B.1.1.7 and one of 3 RBD mutations in B.1.351) nor K417N (one of 3 RBD mutations in B.1.351) disrupted the binding affinity of N-612-017. E484K—an escape mutant found in many different variants, including B.1.351 and A.VOI.V2 (Oliveira et al., 2021; Tegally et al., 2021; Weisblum et al., 2020)—did, however, reduce the binding affinity of N-612-017 by 6- to 10-fold (Figures 6A and 6B). Furthermore, the L452R

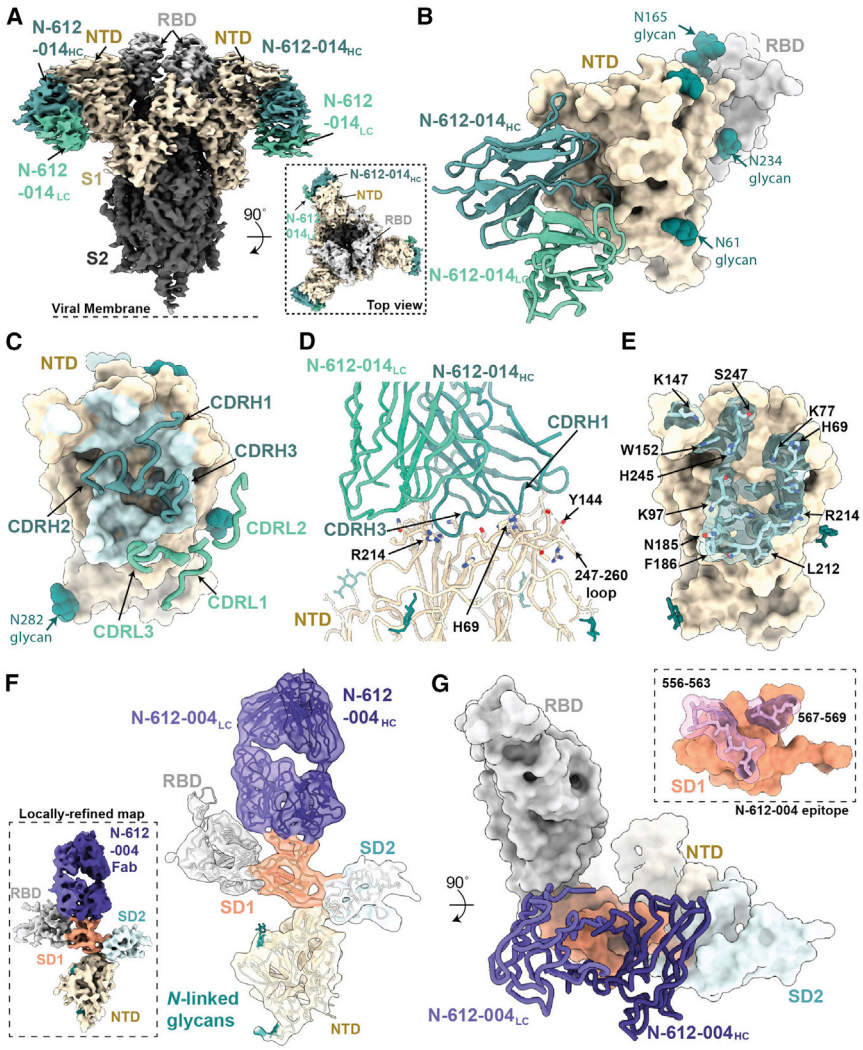

Figure 5. Structures of S1-specific antibodies N-612-014 and N-612-004 bound to SARS-CoV-2 S

(A) Cryo-EM structure of the N-612-014-S trimer complex. Inset: top-down view of the complex.

(B) Close-up view of the N-612-014 variable domains (teal green) contacting the NTD (tan surface). The RBD (gray surface) of an adjacent protomer is shown as a reference.

(C) N-612-014 CDR loops (green ribbons) mapped onto the surface of the NTD (tan surface).

(D) Cartoon representation of the N-612-014-NTD interface.

(E) Surface and stick representations of the N-612-014 epitope (light green surface).

(F) Cryo-EM structure of the N-612-004-S1 protomer (inset) rigid body fit with individual S1 domains (cartoon).

(G) Cartoon and surface representations of N-612-004 (purple) recognition of the SD1 domain. Inset: N-612-004 epitope (pink sticks) highlighted on the SD1 surface (orange). Given the low resolution, epitope residues were assigned using a criterion of a distance of ≤7 Å between antibody-antigen Cα atoms.

mutation found in CA.20C (also known as B.1.1.427 and B.1.1.429) completely abolished the binding of RBD by N-612-017.

N-612-017 and N-612-056 were then evaluated in a pseudovirus neutralization assay (Crawford et al., 2020) using wild-type (containing D614G), B.1.1.7, and B.1.351 pseudoviruses. N-612-017 neutralized wild-type (D614G) and B.1.1.7 pseudoviruses with IC_{50} = 0.09–0.25 μg/mL but failed to neutralize B.1.351. N-612-056 retained neutralization activity against all variants with IC_{50} of 2–10 μg/mL as expected (Figure 6C).

The binding affinity of N-612-014 and N-612-004 against the recombinant S1 domain containing B.1.1.7 mutations was tested, and it was determined that 69-70del and Y144del on NTD did not affect the binding affinity of N-612-014 for S1, whereas these mutations moderately lowered (by about 3-fold) the binding affinity of N-612-004 for S1 (Figures S5B and S5C).

Generation of E484K- and L452R-resistant N-612-017

To recover N-612-017 binding against RBD with the E484K substitution (RBD-E484K), we used an mRNA-doped library for affinity maturation and identified mutations on VH framework 3 (Arg 71 → Ser) and CDR H3 (Asp 97 → Glu) that restored binding affinity against RBD-E484K. The N-612-017 subclone N-612-017-01 containing a single VH: R71S mutation and subclone N-612-017-03 containing double VH:R71S/D97E mutations were tested by BLI for their binding of RBD-B.1.351 and RBD-L452R. Interestingly, both N-612-017-01 and N-612-017-03 subclones not only exhibited restored binding affinity against E484K-expressing RBD variants, but they had 10- to 20-fold enhanced affinity against wild-type RBD (Figures 7A and 7B; Table S7). While neither subclone displayed a complete recovery of binding affinity against RBD-L452R, affinity was relatively enhanced (K_D = 33.1–58.7 nM). These subclones were then tested in a live virus neutralization assay against wild-type (D614G) and B.1.351 viruses and showed neutralization activity against both, whereas the parent N-612-017 did not show neutralization activity against B.1.351 (Figures 7C and 7D).

Subsequently, we used N-612-017-001 in affinity maturation against RBD-L452R and identified 2 clones with restored affinity against RBD-L452R. N-612-017-5B02 containing 4 additional VH mutations (A33T/S54W/G54Δ/S55T) and N-612-017-5B05 containing 4 additional VH mutations (S31P/A33V/R96E/D97E) were tested by BLI for their binding of B.1.351 and RBD-L452R. Both subclones showed a complete recovery of binding affinity against RBD-B.1.351 and RBD-L452R (Figures 7A and 7B; Table S7).

Affinity maturation of N-612-056

To improve potency of N-612-056, we utilized mRNA display for affinity maturation and identified N-612-056-21 containing a

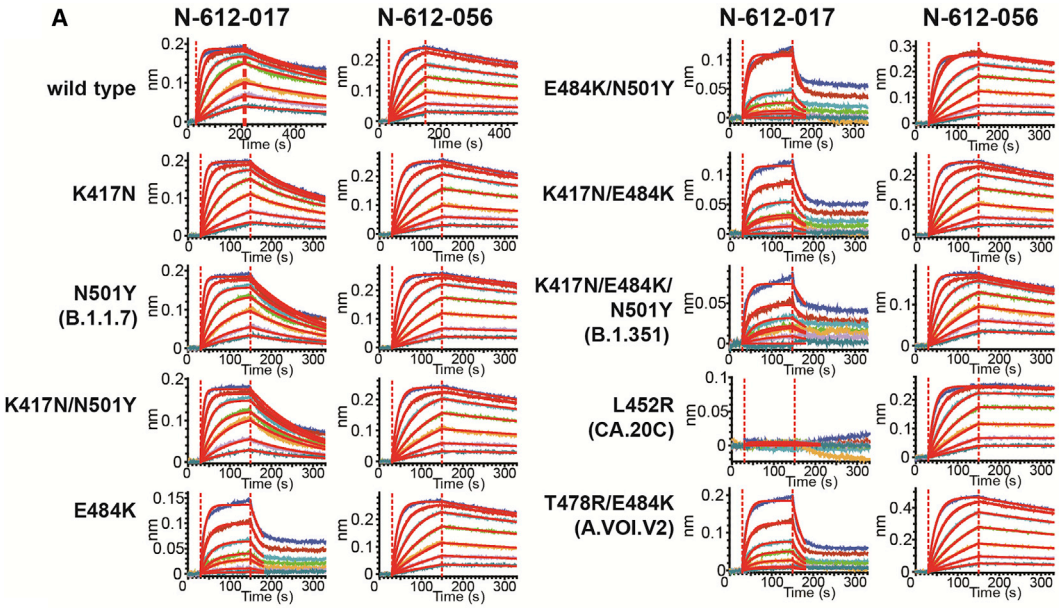

B

RBD mutants	N-612-017 k_{on} (1/Ms)	N-612-017 k_{off} (1/s)	N-612-017 K_D (nM)	N-612-056 k_{on} (1/Ms)	N-612-056 k_{off} (1/s)	N-612-056 K_D (nM)
Wild type	6.77E+05	3.58E-03	5.29	3.37E+05	1.01E-03	2.98
K417N	6.98E+05	3.79E-03	5.45	3.26E+05	1.14E-03	3.49
N501Y (B.1.1.7)	8.35E+05	6.05E-03	7.25	3.88E+05	7.44E-04	1.92
K417N/N501Y	8.87E+05	6.63E-03	7.47	3.62E+05	1.01E-03	2.78
E484K	4.14E+05	2.06E-02	49.7*	3.82E+05	9.64E-04	2.52
E484K/N501Y	4.62E+05	2.92E-02	63.1*	4.04E+05	7.74E-04	1.92
K417N/E484K	4.15E+05	2.35E-02	56.5*	3.55E+05	1.17E-03	3.31
K417N/E484K/N501Y (B.1.351)	4.45E+05	1.36E-02	30.6*	5.19E+05	1.26E-03	2.43
L452R (CA.20C)	N/D	N/D	No binding	5.11E+05	7.38E-04	1.44
T478R/E484K (A.VOI.2)	4.03E+05	2.44E-02	60.7*	2.76E+05	1.05E-03	3.79

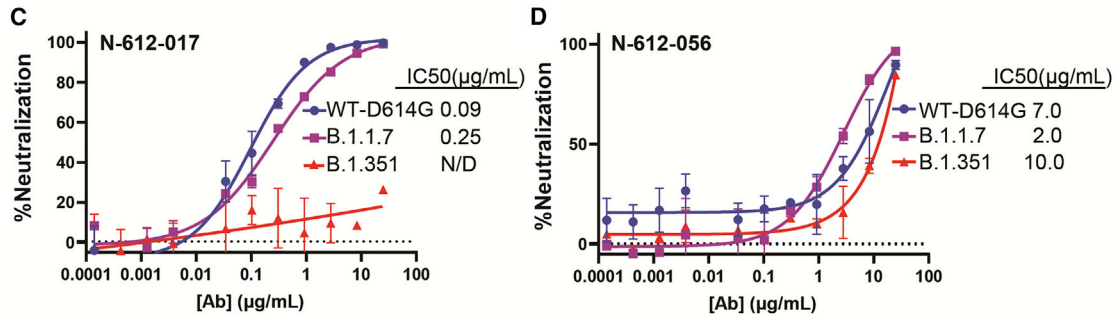

Figure 6. Binding affinity and neutralization activity of N-612-017 and N-612-056 against known SARS-CoV-2 variants

(A) BLI kinetic analysis of N-612-017 and N-612-056 affinity against various mutations found in SARS-CoV-2 variants alone or in combination. N-612-017 binding curves against RBD mutants containing E484K were fit with a 1:1 binding model using a shorter dissociation time (30 s) to highlight weakened binding.

(B) Table of BLI kinetic assay values. SARS-CoV-2 pseudovirus neutralization assay of antibodies. Asterisk indicates K_D values obtained from processing the data with a shorter dissociation time to fit the curves to a 1:1 binding and may not represent accurate K_D.

(C and D) N-612-017 (C) and N-612-056 (D) against wild-type (D614G), (B)1.1.7, and (B)1.351 variants. Mean and standard deviation of duplicate experiments (n = 4) are shown.

single point mutation in VH CDR3 (Ser 99 → Pro) that resulted in a 10-fold improvement in binding affinity (K_D = 0.41 nM) (Figure 7E).

Affinity-matured N-612-017-5B05 and N-612-056-21 were tested against all variants of concern (VOCs) and variants of interest (VOIs) using BLI. N-612-017-5B05 showed a binding

A

Ab	CDRH1 (26-35)	CDRH2 (50-58)	FW H3 (69-73)	CDRH3 (93-101)	CDRL3 (89-86)
N-612-017	GFTFSSYAMH	AIWGSGSNTY	ISRDN	ARGRDLAAFTKTA	QQHDALPW
N-612-017-01	GFTFSSYAMH	AIWGSGSNTY	IS**S**DN	ARGRDLAAFTKTA	QQHDALPW
N-612-017-03	GFTFSSYAMH	AIWGSGSNTY	IS**S**DN	ARGR**E**LAAFTKTA	QQHDALPW
N-612-017-5B02	GFTFSSY**T**MH	AIWG**W**_TNTY	IS**S**DN	ARGRDLAAFTKTA	QQHDALPW
N-612-017-5B05	GFTFS**PY**V**M**H	AIWGSGSNTY	IS**S**DN	ARG**EE**LAAFTKTA	QQHDALPW

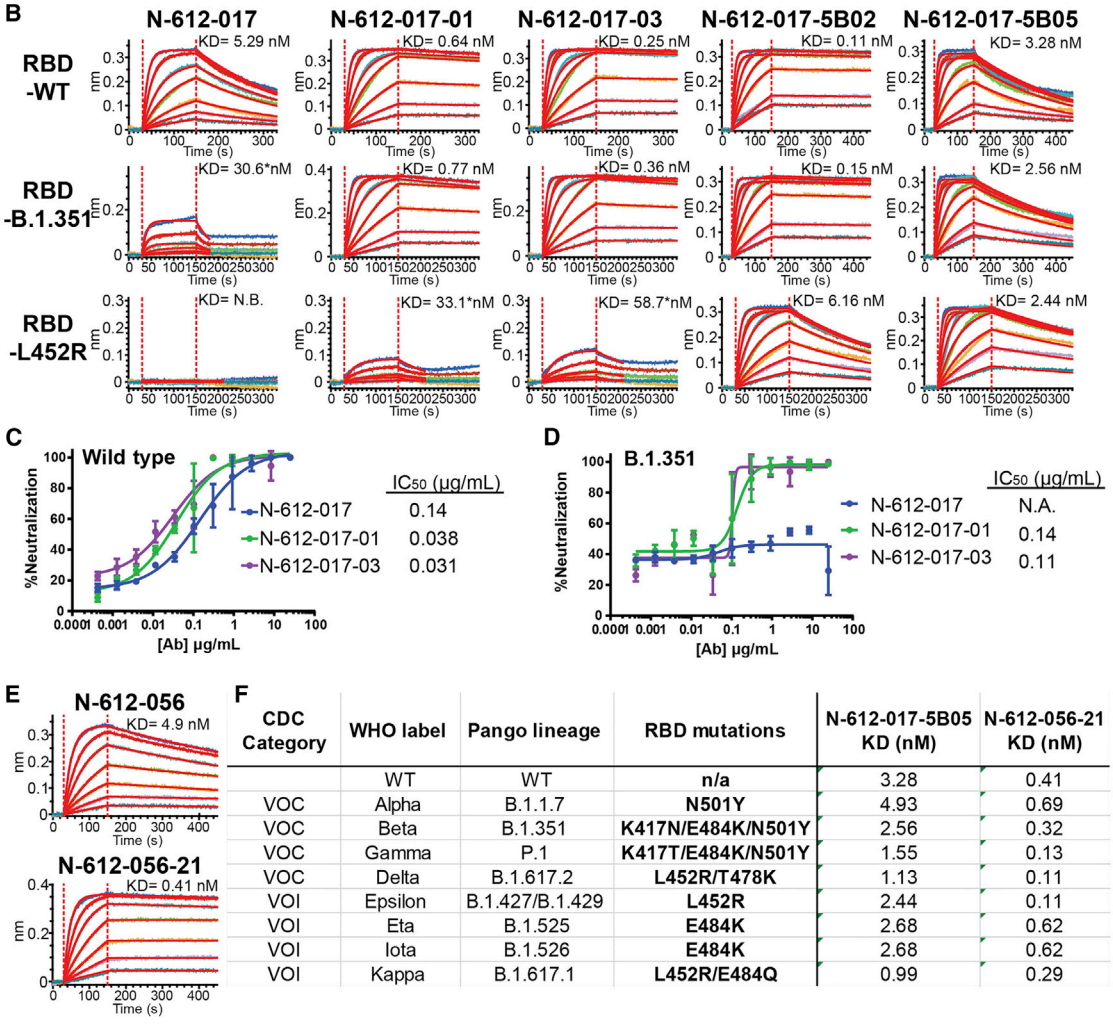

F

CDC Category	WHO label	Pango lineage	RBD mutations	N-612-017-5B05 KD (nM)	N-612-056-21 KD (nM)
	WT	WT	**n/a**	3.28	0.41
VOC	Alpha	B.1.1.7	**N501Y**	4.93	0.69
VOC	Beta	B.1.351	**K417N/E484K/N501Y**	2.56	0.32
VOC	Gamma	P.1	**K417T/E484K/N501Y**	1.55	0.13
VOC	Delta	B.1.617.2	**L452R/T478K**	1.13	0.11
VOI	Epsilon	B.1.427/B.1.429	**L452R**	2.44	0.11
VOI	Eta	B.1.525	**E484K**	2.68	0.62
VOI	Iota	B.1.526	**E484K**	2.68	0.62
VOI	Kappa	B.1.617.1	**L452R/E484Q**	0.99	0.29

Figure 7. Affinity maturation of N-612-017 and N-612-056

(A) VH and VL sequences of N-612-017 affinity-matured subclones

(B) BLI kinetic analysis of N-612-017 affinity-matured subclones against RBD-wild type, RBD-B.1.351, and RBD-L452R. Asterisk indicates K_D values obtained from processing the data with a shorter dissociation time to fit the curves to a 1:1 binding model and may not represent accurate K_D values.

(C and D) SARS-CoV-2 live virus neutralization assay of N-612-017, N-617-017-01, and N-612-017-03 against (C) wild-type and (D) (B)1.351 variants. Mean and standard deviation of duplicate experiments (n = 3) are shown.

(E) BLI kinetic analysis of N-612-056 and affinity-matured N-612-056-21 against RBD-wild type.

(F) Table of binding affinity of N-612-017-5B05 and N-612-056-21 against the RBD containing variant mutations from all the VOCs and VOIs listed by the Centers for Disease Control and Prevention (CDC).

affinity to the variants that was similar to the parent molecule N-612-017, whereas N-612-056-21 displayed binding affinities that were improved as much as ~10-fold compared with N-612-056 (Figure 7F).

DISCUSSION

Our use of *in vitro* mRNA display facilitated our identification of antibody sequences and enabled us to enhance their binding

affinity for the mutated S of SARS-CoV-2 variants through affinity maturation. BLI and epitope binning analysis determined that the 10 IgG1 antibody sequences identified here bind 7 distinct epitope regions on the SARS-CoV-2 S protein. Major sequence differences in CDRH3 and CDRL3 loops in combination with minor variations in CDRH1 and CDRH2 can drive the recognition of a broad spectrum of epitopes and create potent neutralizing interactions with the SARS-CoV-2 S protein. Previous immunoglobulin heavy chain variable region (IGHV) gene analysis identified distinct IGVH genes (e.g. 1–53) that were more likely to produce potent RBD-binding nAbs (Dejnirattisai et al., 2021; Robbiani et al., 2020; Yuan et al., 2020) within the human antibody repertoire. The nAb N-612-017 VH sequence is most similar to IGHV 3–23, which are most abundant in human antibodies, and shows potent neutralizing activity (<0.1 μg/mL), suggesting that CDR sequence variation is essential in determining potency against antigens regardless of germline genes.

The majority of potent nAbs (~90%) are RBD targeting, and the remainder target the NTD of the S protein (Brouwer et al., 2020; Cao et al., 2020; Liu et al., 2020; McCallum et al., 2021b). Our most potent nAb N-612-017 is RBD targeting and is categorized into class 2, as characterized by cryo-EM. Though N-612-056 also neutralized SARS-CoV-2 by targeting the RBD, albeit at lower potency, it lacks the ability to directly block ACE2 binding and binds to a cryptic epitope on the RBD. Similar antibody binding to this cryptic epitope by a patient-derived antibody has been previously reported (Dejnirattisai et al., 2021). The rarity of this epitope is evident in the convalescent plasma blocking assay, in which convalescent plasma from 3 out 4 patients failed to block N-612-056 from binding to the S protein. This cryptic interface is well conserved, and although the potency of N-612-056 is relatively low, cross-reactivity with the SARS-CoV RBD and the sustained binding affinity for the mutant SARS-CoV-2 RBD found in circulating variants suggests that N-612-056 may be an attractive mAb therapy candidate against novel variants.

The cryo-EM structural data presented here reveal that N-612-014 binds the NTD at a site different from that of the majority of described antibodies (McCallum et al., 2021b), suggesting the presence of a second neutralization site on the NTD. Proposed mechanisms for nAbs targeting the NTD include destabilization of the S trimer by S1 shedding and blockage of cell-cell fusion auxiliary receptor binding, membrane fusion, or proteolytic activation (Huo et al., 2020; Walls et al., 2019; Wec et al., 2020; Wrobel et al., 2020). N-612-014 displayed neutralization activity in live virus assays, whereas it lacked neutralization activity in a pseudovirus assay. Although this type of discrepancy is rare, such inter-assay discrepancies have been described previously (Liu et al., 2020). N-612-014 may require a longer incubation time to reach maximum neutralization because this allows the opportunity for the S trimer to adopt a conformation that is more susceptible to S1 shedding that is promoted by the antibody, thus destabilizing S; this hypothesis awaits experimental confirmation.

The SD1-targeting antibody N-612-004 displayed partial neutralization activity and was only observed in complex with an S1 domain dissociated from the S trimer in cryo-EM. To our knowledge, there have been no reports on SD1-targeting antibodies that display neutralization activity. We also identified the S2-targeting antibody N-612-007 that displayed partial neutralization activity in a live virus neutralization assay, and while structural analysis was attempted, we were unable to visualize/characterize an S trimer-N-612-007 complex. nAbs targeting S2 domain have been previously observed in Middle East respiratory syndrome (MERS)-CoV and SARS-CoV (Elshabrawy et al., 2012; Lai et al., 2005; Lip et al., 2006; Pallesen et al., 2017), and recently reported structures of an SARS-CoV-2 S2-antibody complex have also revealed antibody binding to the S2 stem helix, which may interfere with membrane fusion machinery (Zhou et al., 2021). Other S2 epitope regions identified for SARS-CoV nAbs are two heptad repeat regions essential in cell fusion during virus entry (Elshabrawy et al., 2012; Lip et al., 2006; Pallesen et al., 2017). Neutralization activities of these non-RBD binders (N-612-014, N-612-004, and N-612-007) were inconsistent between multiple assays and generally not very potent when tested individually. However, when tested in combination with N-612-017, all of them slightly enhanced the neutralization activity of N-612-017. This may suggest a role of non-RBD binding antibodies in neutralization.

Bamlanivimab is a class 2 RBD binder that neutralizes wild-type SARS-CoV-2 and was the first antibody to attain emergency use authorization (EUA) by the FDA (Jones et al., 2021). This EUA was, however, recently revoked due to the loss of potency against SARS-CoV-2 variants (Widera et al., 2021). Two alternate mAb therapies remain available under EUA: a combination of casirivimab plus imdevimab (Baum et al., 2020; Pinto et al., 2020) and combination of bamlanivimab plus etesevimab. In both cases, administering 2 mAbs together is the key to compounding potency and reducing the risk of variant virus escape from neutralization. Our N-612-017 antibody is a class 2 RBD binder similar to bamlanivimab that also displays a loss of activity in the presence of the E484K mutation. To address this potential loss of efficacy, we used affinity maturation for N-612-017 and quickly identified subclones that restored affinity for both E484K and L452R. N-612-056 is resistant to all RBD variants, and N-612-014 is not affected by the NTD mutation present in B.1.1.7. These nAbs are attractive candidates for use in combination with N-612-017. N-612-056 was quickly affinity-matured to present an attractive combo approach in combination with N-612-017 to combat variants.

The recent emergence of more transmissible and infectious variants such as B.1.351 (Beta) and B.1.617 (Delta) highlights the need for a method to rapidly address mutations that overcome current therapies and existing immunity. The results described in this study demonstrate the utility of mRNA-display-based nAb discovery in the identification of antiviral mAbs against the rapidly evolving SARS-CoV-2 pathogen, which should be applicable to other novel or seasonal pathogens.

Limitations of the study

Although we identified several nAbs showing neutralization activity against SARS-CoV-2 virus and rapidly affinity-matured the best clones to be variant-resistant using mRNA display technology, a major unanswered question is whether these nAbs will have efficacy in *in vivo* studies. Based on K_D values obtained in BLI and on IC_{50} values in live virus neutralization assays, we anticipate that they will have activity in *in vivo*; however, it remains to be tested. Further, while we determined it was outside the scope of

the current paper, we did not generate/analyze crystal structures of an escape variant such as RBD-E484K in complex with antibodies N-612-017-01/03 in comparison with N-612-017. Such analyses may be performed as part of future studies.

STAR★METHODS

Detailed methods are provided in the online version of this paper and include the following:

- KEY RESOURCES TABLE
- RESOURCE AVAILABILITY
  - Lead contact
  - Materials availability
  - Data and code availability
- EXPERIMENTAL MODEL AND SUBJECT DETAILS
- METHOD DETAILS
  - mRNA display
  - Production antibodies and recombinant SARS-CoV-2 S domains
  - Bio-layer interferometry (BLI) kinetic analysis of antibodies
  - ACE2 blocking assay
  - Epitope binning
  - Developability assays
  - Convalescent plasma blocking assay
  - Vero E6 neutralization assay
  - Pseudovirus neutralization assays
  - Cryo-EM sample preparation
  - Cryo-EM structure determination of N-612-004, N-612-014, and N-612-017 Fab in complex with S-6P
  - X-Ray crystallography structure determination of N-612-056 in complex with RBD
  - Structure analyses
- QUANTIFICATION AND STATISTICAL ANALYSIS

SUPPLEMENTAL INFORMATION

Supplemental information can be found online at https://doi.org/10.1016/j.celrep.2022.110348.

ACKNOWLEDGMENTS

We thank J. Vielmetter, P. Hoffman, and the Protein Expression Center in the Beckman Institute at Caltech for expression assistance and K. Huey-Tubman for assistance with soluble spike purification. Electron microscopy was performed in the Caltech Cryo-EM Center with assistance from S. Chen and A. Malyutin. We thank the Gordon and Betty Moore and Beckman Foundations for gifts to Caltech to support the Molecular Observatory. We thank J. Kaiser, director of the Molecular Observatory at Caltech, and beamline staff C. Smith and S. Russi at SSRL for data collection assistance. Use of the Stanford Synchrotron Radiation Lightsource, SLAC National Accelerator Laboratory, is supported by the US Department of Energy Office of Science, Office of Basic Energy Sciences under contract no. DE-AC02-76SF00515. The SSRL Structural Molecular Biology Program is supported by the DOE Office of Biological and Environmental Research and by the National Institutes of Health, National Institute of General Medical Sciences (P30GM133894). The contents of this publication are solely the responsibility of the authors and do not necessarily represent the official views of NIGMS or NIH. This work was supported by NIH (P01-AI138938-S1 to P.J.B.), the Caltech Merkin Institute for Translational Research (P.J.B.), and a George Mason University Fast Grant (P.J.B.). C.O.B was supported by the Hanna Gray Fellowship Program from the Howard Hughes Medical Institute and the Postdoctoral Enrichment Program from the Burroughs Wellcome Fund. This work was also supported by ImmunityBio, Inc.

AUTHOR CONTRIBUTIONS

Experimental designs, C.A.O., S.T., C.O.B., K.N., S.R., and P.S.-S.; mRNA library display, C.A.O.; cloning, C.A.O. and W.H.; protein expression and purification, C.A.O., S.T., and M.G.; kinetic analysis, ACE2 blocking assay, epitope binning, and convalescent plasma blocking assay, S.T.; developability assays M.G. and S.T.; cryo-EM and X-ray crystallography, C.O.B. and P.J.B.; Vero E6 live virus neutralization assay, J.T., A.R., M.M.-F., and D.B.; pseudovirus neutralization assay, P.G.; manuscript preparation, S.T., C.O.B., C.A.O., and P.S.

DECLARATION OF INTERESTS

C.A.O., S.T., W.H., K.N., and P.S.-S. are inventors for an international patent application with this work (US 11,015,188 B2). M.G. and P.S. are employees of ImmunityBio, Inc., and S.R. was a former employee and is a current shareholder of ImmunityBio, Inc.

Received: September 17, 2021
Revised: December 6, 2021
Accepted: January 14, 2022
Published: February 08, 2022

REFERENCES

Adams, P.D., Afonine, P.V., Bunkóczi, G., Chen, V.B., Davis, I.W., Echols, N., Headd, J.J., Hung, L.-W., Kapral, G.J., Grosse-Kunstleve, R.W., et al. (2010). PHENIX: a comprehensive Python-based system for macromolecular structure solution. Acta Crystallogr. D Biol. Crystallogr. *66*, 213–221.

Barnes, C.O., West, A.P., Huey-Tubman, K.E., Hoffmann, M.A.G., Sharaf, N.G., Hoffman, P.R., Koranda, N., Gristick, H.B., Gaebler, C., Muecksch, F., et al. (2020a). Structures of human antibodies bound to SARS-CoV-2 spike reveal common epitopes and recurrent features of antibodies. Cell *182*, 828–842.e16.

Barnes, C.O., Jette, C.A., Abernathy, M.E., Dam, K.-M.A., Esswein, S.R., Gristick, H.B., Malyutin, A.G., Sharaf, N.G., Huey-Tubman, K.E., Lee, Y.E., et al. (2020b). SARS-CoV-2 neutralizing antibody structures inform therapeutic strategies. Nature *588*, 682–687.

Baum, A., Fulton, B.O., Wloga, E., Copin, R., Pascal, K.E., Russo, V., Giordano, S., Lanza, K., Negron, N., Ni, M., et al. (2020). Antibody cocktail to SARS-CoV-2 spike protein prevents rapid mutational escape seen with individual antibodies. Science *369*, 1014–1018.

Bell, J.M., Chen, M., Baldwin, P.R., and Ludtke, S.J. (2016). High resolution single particle refinement in EMAN2.1. Methods *100*, 25–34.

Brouwer, P.J.M., Caniels, T.G., van der Straten, K., Snitselaar, J.L., Aldon, Y., Bangaru, S., Torres, J.L., Okba, N.M.A., Claireaux, M., Kerster, G., et al. (2020). Potent neutralizing antibodies from COVID-19 patients define multiple targets of vulnerability. Science *369*, 643–650.

Cao, Y., Su, B., Guo, X., Sun, W., Deng, Y., Bao, L., Zhu, Q., Zhang, X., Zheng, Y., Geng, C., et al. (2020). Potent neutralizing antibodies against SARS-CoV-2 identified by high-throughput single-cell sequencing of convalescent patients' B cells. Cell *182*, 73–84.e16.

Cathcart, A.L., Havenar-Daughton, C., Lempp, F.A., Ma, D., Schmid, M.A., Agostini, M.L., Guarino, B., Iulio, J.D., Rosen, L.E., Tucker, H., et al. (2021). The Dual Function Monoclonal Antibodies VIR-7831 and VIR-7832 Demonstrate Potent in Vitro and in Vivo Activity against SARS-CoV-2. BioRxiv. https://doi.org/10.1101/2021.03.09.434607.

Cele, S., Gazy, I., Jackson, L., Hwa, S.-H., Tegally, H., Lustig, G., Giandhari, J., Pillay, S., Wilkinson, E., Naidoo, Y., et al. (2021). Escape of SARS-CoV-2 501Y.V2 from neutralization by convalescent plasma. Nature *593*, 142–146.

Cerutti, G., Guo, Y., Zhou, T., Gorman, J., Lee, M., Rapp, M., Reddem, E.R., Yu, J., Bahna, F., Bimela, J., et al. (2021). Potent SARS-CoV-2 neutralizing

antibodies directed against spike N-terminal domain target a single supersite. Cell Host Microbe *29*, 819–833.e7.

Cohen, A.A., Gnanapragasam, P.N.P., Lee, Y.E., Hoffman, P.R., Ou, S., Kakutani, L.M., Keeffe, J.R., Wu, H.-J., Howarth, M., West, A.P., et al. (2021). Mosaic nanoparticles elicit cross-reactive immune responses to zoonotic coronaviruses in mice. Science *371*, 735–741.

Crawford, K.H.D., Eguia, R., Dingens, A.S., Loes, A.N., Malone, K.D., Wolf, C.R., Chu, H.Y., Tortorici, M.A., Veesler, D., Murphy, M., et al. (2020). Protocol and reagents for pseudotyping lentiviral particles with SARS-CoV-2 spike protein for neutralization assays. Viruses *12*, 513.

Davies, N.G., Abbott, S., Barnard, R.C., Jarvis, C.I., Kucharski, A.J., Munday, J.D., Pearson, C.A.B., Russell, T.W., Tully, D.C., Washburne, A.D., et al. (2021). Estimated transmissibility and impact of SARS-CoV-2 lineage B.1.1.7 in England. Science *372*, eabg3055.

Dejnirattisai, W., Zhou, D., Ginn, H.M., Duyvesteyn, H.M.E., Supasa, P., Case, J.B., Zhao, Y., Walter, T.S., Mentzer, A.J., Liu, C., et al. (2021). The antigenic anatomy of SARS-CoV-2 receptor binding domain. Cell *184*, 2183–2200.e22.

Deng, X., Garcia-Knight, M.A., Khalid, M.M., Servellita, V., Wang, C., Morris, M.K., Sotomayor-González, A., Glasner, D.R., Reyes, K.R., Gliwa, A.S., et al. (2021). Transmission, infectivity, and neutralization of a spike L452R SARS-CoV-2 variant. Cell *184*, 3426–3437.e8.

Elshabrawy, H.A., Coughlin, M.M., Baker, S.C., and Prabhakar, B.S. (2012). Human monoclonal antibodies against highly conserved HR1 and HR2 domains of the SARS-CoV spike protein are more broadly neutralizing. PLoS One *7*, e50366.

Emsley, P., Lohkamp, B., Scott, W.G., and Cowtan, K. (2010). Features and development of Coot. Acta Crystallogr. D Biol. Crystallogr. *66*, 486–501.

Greaney, A.J., Starr, T.N., Gilchuk, P., Zost, S.J., Binshtein, E., Loes, A.N., Hilton, S.K., Huddleston, J., Eguia, R., Crawford, K.H.D., et al. (2021a). Complete mapping of mutations to the SARS-CoV-2 spike receptor-binding domain that escape antibody recognition. Cell Host Microbe *29*, 44–57.e9.

Goddard, T.D., Huang, C.C., Meng, E.C., Pettersen, E.F., Couch, G.S., Morris, J.H., and Ferrin, T.E. (2018). UCSF ChimeraX: Meeting modern challenges in visualization and analysis. Protein Sci *27*, 14–25.

Greaney, A.J., Starr, T.N., Barnes, C.O., Weisblum, Y., Schmidt, F., Caskey, M., Gaebler, C., Cho, A., Agudelo, M., Finkin, S., et al. (2021b). Mapping mutations to the SARS-CoV-2 RBD that escape binding by different classes of antibodies. Nat. Commun. *12*, 4196.

Hansen, J., Baum, A., Pascal, K.E., Russo, V., Giordano, S., Wloga, E., Fulton, B.O., Yan, Y., Koon, K., Patel, K., et al. (2020). Studies in humanized mice and convalescent humans yield a SARS-CoV-2 antibody cocktail. Science *369*, 1010–1014.

Hoffmann, M., Kleine-Weber, H., Schroeder, S., Krüger, N., Herrler, T., Erichsen, S., Schiergens, T.S., Herrler, G., Wu, N.-H., Nitsche, A., et al. (2020). SARS-CoV-2 cell entry depends on ACE2 and TMPRSS2 and is blocked by a clinically proven protease inhibitor. Cell *181*, 271–280.e8.

Huo, J., Zhao, Y., Ren, J., Zhou, D., Duyvesteyn, H.M.E., Ginn, H.M., Carrique, L., Malinauskas, T., Ruza, R.R., Shah, P.N.M., et al. (2020). Neutralization of SARS-CoV-2 by destruction of the prefusion spike. Cell Host Microbe *28*, 445–454.e6.

Hutchison, C.A., Nordeen, S.K., Vogt, K., and Edgell, M.H. (1986). A complete library of point substitution mutations in the glucocorticoid response element of mouse mammary tumor virus. Proc. Natl. Acad. Sci. U S A *83*, 710–714.

Ionescu, R.M., Vlasak, J., Price, C., and Kirchmeier, M. (2008). Contribution of variable domains to the stability of humanized IgG1 monoclonal antibodies. J. Pharm. Sci. *97*, 1414–1426.

Jain, T., Sun, T., Durand, S., Hall, A., Houston, N.R., Nett, J.H., Sharkey, B., Bobrowicz, B., Caffry, I., Yu, Y., et al. (2017). Biophysical properties of the clinical-stage antibody landscape. Proc. Natl. Acad. Sci. U S A *114*, 944–949.

Jones, B.E., Brown-Augsburger, P.L., Corbett, K.S., Westendorf, K., Davies, J., Cujec, T.P., Wiethoff, C.M., Blackbourne, J.L., Heinz, B.A., Foster, D., et al. (2021). The neutralizing antibody, LY-CoV555, protects against SARS-CoV-2 infection in nonhuman primates. Sci. Transl. Med. *13*, eabf1906.

Kabsch, W. (2010). XDS. Acta Crystallogr. D Biol. Crystallogr. *66*, 125–132.

Kirchdoerfer, R.N., Cottrell, C.A., Wang, N., Pallesen, J., Yassine, H.M., Turner, H.L., Corbett, K.S., Graham, B.S., McLellan, J.S., and Ward, A.B. (2016). Pre-fusion structure of a human coronavirus spike protein. Nature *531*, 118–121.

Krissinel, E., and Henrick, K. (2007). Inference of macromolecular assemblies from crystalline state. J. Mol. Biol. *372*, 774–797.

Kuzmina, A., Khalaila, Y., Voloshin, O., Keren-Naus, A., Boehm-Cohen, L., Raviv, Y., Shemer-Avni, Y., Rosenberg, E., and Taube, R. (2021). SARS-CoV-2 spike variants exhibit differential infectivity and neutralization resistance to convalescent or post-vaccination sera. Cell Host Microbe *29*, 522–528.e2.

Lai, S.-C., Chong, P.C.-S., Yeh, C.-T., Liu, L.S.-J., Jan, J.-T., Chi, H.-Y., Liu, H.-W., Chen, A., and Wang, Y.-C. (2005). Characterization of neutralizing monoclonal antibodies recognizing a 15-residues epitope on the spike protein HR2 region of severe acute respiratory syndrome coronavirus (SARS-CoV). J. Biomed. Sci. *12*, 711–727.

Li, W., Moore, M.J., Vasilieva, N., Sui, J., Wong, S.K., Berne, M.A., Somasundaran, M., Sullivan, J.L., Luzuriaga, K., Greenough, T.C., et al. (2003). Angiotensin-converting enzyme 2 is a functional receptor for the SARS coronavirus. Nature *426*, 450–454.

Li, Z., Tomlinson, A.C., Wong, A.H., Zhou, D., Desforges, M., Talbot, P.J., Benlekbir, S., Rubinstein, J.L., and Rini, J.M. (2019). The human coronavirus HCoV-229E S-protein structure and receptor binding. ELife *8*, e51230.

Liao, H.-I., Olson, C.A., Hwang, S., Deng, H., Wong, E., Baric, R.S., Roberts, R.W., and Sun, R. (2009). mRNA display design of fibronectin-based intrabodies that detect and inhibit severe acute respiratory syndrome coronavirus nucleocapsid protein. J. Biol. Chem. *284*, 17512–17520.

Lip, K.-M., Shen, S., Yang, X., Keng, C.-T., Zhang, A., Oh, H.-L.J., Li, Z.-H., Hwang, L.-A., Chou, C.-F., Fielding, B.C., et al. (2006). Monoclonal antibodies targeting the HR2 domain and the region immediately upstream of the HR2 of the S protein neutralize in vitro infection of severe acute respiratory syndrome coronavirus. J. Virol. *80*, 941–950.

Liu, L., Wang, P., Nair, M.S., Yu, J., Rapp, M., Wang, Q., Luo, Y., Chan, J.F.-W., Sahi, V., Figueroa, A., et al. (2020). Potent neutralizing antibodies against multiple epitopes on SARS-CoV-2 spike. Nature *584*, 450–456.

Liu, R., Barrick, J.E., Szostak, J.W., and Roberts, R.W. (2000). Optimized synthesis of RNA-protein fusions for in vitro protein selection. Methods Enzymol. *318*, 268–293.

Mastronarde, D.N. (2005). Automated electron microscope tomography using robust prediction of specimen movements. J. Struct. Biol. *152*, 36–51.

McCallum, M., Bassi, J., Marco, A.D., Chen, A., Walls, A.C., Iulio, J.D., Tortorici, M.A., Navarro, M.-J., Silacci-Fregni, C., Saliba, C., et al. (2021a). SARS-CoV-2 immune evasion by the B.1.427/B.1.429 variant of concern. Science *373*, 648–654.

McCallum, M., Marco, A.D., Lempp, F.A., Tortorici, M.A., Pinto, D., Walls, A.C., Beltramello, M., Chen, A., Liu, Z., Zatta, F., et al. (2021b). N-terminal domain antigenic mapping reveals a site of vulnerability for SARS-CoV-2. Cell *184*, 2332–2347.e16.

McCarthy, K.R., Rennick, L.J., Nambulli, S., Robinson-McCarthy, L.R., Bain, W.G., Haidar, G., and Duprex, W.P. (2021). Recurrent deletions in the SARS-CoV-2 spike glycoprotein drive antibody escape. Science *371*, 1139–1142.

McCoy, A.J., Grosse-Kunstleve, R.W., Adams, P.D., Winn, M.D., Storoni, L.C., and Read, R.J. (2007). Phaser crystallographic software. J. Appl. Crystallogr. *40*, 658–674.

Newton, M.S., Cabezas-Perusse, Y., Tong, C.L., and Seelig, B. (2020). In vitro selection of peptides and proteins advantages of mRNA display. ACS Synth. Biol. *9*, 181–190.

Oliveira, T.D., Lutucuta, S., Nkengasong, J., Morais, J., Paixão, J.P., Neto, Z., Afonso, P., Miranda, J., David, K., Inglês, L., et al. (2021). A novel variant of interest of SARS-CoV-2 with multiple spike mutations detected through travel surveillance in Africa. MedRxiv. https://doi.org/10.1101/2021.03.30.21254323.

Olson, C.A. (2021). mRNA display antibody library and methods. US *11*, 015,188 B2.

Olson, C.A., Liao, H.-I., Sun, R., and Roberts, R.W. (2008). mRNA display selection of a high-affinity, modification-specific phospho-IκBα-binding fibronectin. ACS Chem. Biol. *3*, 480–485.

Olson, C.A., Adams, J.D., Takahashi, T.T., Qi, H., Howell, S.M., Wu, T.-T., Roberts, R.W., Sun, R., and Soh, H.T. (2011). Rapid mRNA-display selection of an IL-6 inhibitor using continuous-flow magnetic separation. Angew. Chem. Int. Ed. Engl. *50*, 8295–8298.

Pallesen, J., Wang, N., Corbett, K.S., Wrapp, D., Kirchdoerfer, R.N., Turner, H.L., Cottrell, C.A., Becker, M.M., Wang, L., Shi, W., et al. (2017). Immunogenicity and structures of a rationally designed prefusion MERS-CoV spike antigen. Proc. Natl. Acad. Sci. U S A *114*, E7348–E7357.

Piccoli, L., Park, Y.-J., Tortorici, M.A., Czudnochowski, N., Walls, A.C., Beltramello, M., Silacci-Fregni, C., Pinto, D., Rosen, L.E., Bowen, J.E., et al. (2020). Mapping neutralizing and immunodominant sites on the SARS-CoV-2 spike receptor-binding domain by structure-guided high-resolution serology. Cell *183*, 1024–1042.e21.

Pinto, D., Park, Y.-J., Beltramello, M., Walls, A.C., Tortorici, M.A., Bianchi, S., Jaconi, S., Culap, K., Zatta, F., De Marco, A., et al. (2020). Cross-neutralization of SARS-CoV-2 by a human monoclonal SARS-CoV antibody. Nature *583*, 290–295.

Plante, J.A., Liu, Y., Liu, J., Xia, H., Johnson, B.A., Lokugamage, K.G., Zhang, X., Muruato, A.E., Zou, J., Fontes-Garfias, C.R., et al. (2021). Spike mutation D614G alters SARS-CoV-2 fitness. Nature *592*, 116–121.

Punjani, A., Rubinstein, J.L., Fleet, D.J., and Brubaker, M.A. (2017). cryoSPARC: algorithms for rapid unsupervised cryo-EM structure determination. Nat. Methods *14*, 290–296.

Ribes, M., Chaccour, C., and Moncunill, G. (2021). Adapt or perish: SARS-CoV-2 antibody escape variants defined by deletions in the Spike N-terminal Domain. Signal Transduct. Target. Ther. *6*, 1–2.

Robbiani, D.F., Gaebler, C., Muecksch, F., Lorenzi, J.C.C., Wang, Z., Cho, A., Agudelo, M., Barnes, C.O., Gazumyan, A., Finkin, S., et al. (2020). Convergent antibody responses to SARS-CoV-2 in convalescent individuals. Nature *584*, 437–442.

Roberts, R.W., and Szostak, J.W. (1997). RNA-peptide fusions for the in vitro selection of peptides and proteins. Proc. Natl. Acad. Sci. *94*, 12297–12302.

Starr, T.N., Greaney, A.J., Hilton, S.K., Ellis, D., Crawford, K.H.D., Dingens, A.S., Navarro, M.J., Bowen, J.E., Tortorici, M.A., Walls, A.C., et al. (2020). Deep mutational scanning of SARS-CoV-2 receptor binding domain reveals constraints on folding and ACE2 binding. Cell *182*, 1295–1310.e20.

Starr, T.N., Greaney, A.J., Addetia, A., Hannon, W.W., Choudhary, M.C., Dingens, A.S., Li, J.Z., and Bloom, J.D. (2021). Prospective mapping of viral mutations that escape antibodies used to treat COVID-19. Science *371*, 850–854.

Suryadevara, N., Shrihari, S., Gilchuk, P., VanBlargan, L.A., Binshtein, E., Zost, S.J., Nargi, R.S., Sutton, R.E., Winkler, E.S., Chen, E.C., et al. (2021). Neutralizing and protective human monoclonal antibodies recognizing the N-terminal domain of the SARS-CoV-2 spike protein. Cell *184*, 2316–2331.e15.

Takahashi, T.T., Austin, R.J., and Roberts, R.W. (2003). mRNA display: ligand discovery, interaction analysis and beyond. Trends Biochem. Sci. *28*, 159–165.

Tegally, H., Wilkinson, E., Giovanetti, M., Iranzadeh, A., Fonseca, V., Giandhari, J., Doolabh, D., Pillay, S., San, E.J., Msomi, N., et al. (2021). Detection of a SARS-CoV-2 variant of concern in South Africa. Nature *592*, 438–443.

Walls, A.C., Tortorici, M.A., Bosch, B.-J., Frenz, B., Rottier, P.J.M., DiMaio, F., Rey, F.A., and Veesler, D. (2016). Cryo-electron microscopy structure of a coronavirus spike glycoprotein trimer. Nature *531*, 114–117.

Walls, A.C., Xiong, X., Park, Y.-J., Tortorici, M.A., Snijder, J., Quispe, J., Cameroni, E., Gopal, R., Dai, M., Lanzavecchia, A., et al. (2019). Unexpected receptor functional mimicry elucidates activation of coronavirus fusion. Cell *176*, 1026–1039.e15.

Walls, A.C., Park, Y.-J., Tortorici, M.A., Wall, A., McGuire, A.T., and Veesler, D. (2020). Structure, function, and antigenicity of the SARS-CoV-2 spike glycoprotein. Cell *181*, 281–292.e6.

Wang, P., Nair, M.S., Liu, L., Iketani, S., Luo, Y., Guo, Y., Wang, M., Yu, J., Zhang, B., Kwong, P.D., et al. (2021). Antibody resistance of SARS-CoV-2 variants B.1.351 and B.1.1.7. Nature *593*, 130–135.

Wec, A.Z., Wrapp, D., Herbert, A.S., Maurer, D.P., Haslwanter, D., Sakharkar, M., Jangra, R.K., Dieterle, M.E., Lilov, A., Huang, D., et al. (2020). Broad neutralization of SARS-related viruses by human monoclonal antibodies. Science *369*, 731–736.

Weinreich, D.M., Sivapalasingam, S., Norton, T., Ali, S., Gao, H., Bhore, R., Musser, B.J., Soo, Y., Rofail, D., Im, J., et al. (2021). REGN-COV2, a neutralizing antibody cocktail, in outpatients with covid-19. N. Engl. J. Med. *384*, 238–251.

Weisblum, Y., Schmidt, F., Zhang, F., DaSilva, J., Poston, D., Lorenzi, J.C., Muecksch, F., Rutkowska, M., Hoffmann, H.-H., Michailidis, E., et al. (2020). Escape from neutralizing antibodies by SARS-CoV-2 spike protein variants. ELife *9*, e61312.

Widera, M., Wilhelm, A., Hoehl, S., Pallas, C., Kohmer, N., Wolf, T., Rabenau, H.F., Corman, V., Drosten, C., Vehreschild, M.J., et al. (2021). Bamlanivimab does not neutralize two SARS-CoV-2 variants carrying E484K in vitro. MedRxiv. https://doi.org/10.1101/2021.02.24.21252372.

Winn, M.D., Ballard, C.C., Cowtan, K.D., Dodson, E.J., Emsley, P., Evans, P.R., Keegan, R.M., Krissinel, E.B., Leslie, A.G.W., McCoy, A., et al. (2011). Overview of the CCP4 suite and current developments. Acta Crystallogr. D Biol. Crystallogr. *67*, 235–242.

Wrapp, D., Wang, N., Corbett, K.S., Goldsmith, J.A., Hsieh, C.-L., Abiona, O., Graham, B.S., and McLellan, J.S. (2020). Cryo-EM structure of the 2019-nCoV spike in the prefusion conformation. Science *367*, 1260–1263.

Wrobel, A.G., Benton, D.J., Xu, P., Roustan, C., Martin, S.R., Rosenthal, P.B., Skehel, J.J., and Gamblin, S.J. (2020). SARS-CoV-2 and bat RaTG13 spike glycoprotein structures inform on virus evolution and furin-cleavage effects. Nat. Struct. Mol. Biol. *27*, 763–767.

Yuan, M., Liu, H., Wu, N.C., Lee, C.-C.D., Zhu, X., Zhao, F., Huang, D., Yu, W., Hua, Y., Tien, H., et al. (2020). Structural basis of a shared antibody response to SARS-CoV-2. Science *369*, 1119–1123.

Yuan, M., Huang, D., Lee, C.-C.D., Wu, N.C., Jackson, A.M., Zhu, X., Liu, H., Peng, L., van Gils, M.J., Sanders, R.W., et al. (2021). Structural and functional ramifications of antigenic drift in recent SARS-CoV-2 variants. Science *373*, 818–823.

Yuan, Y., Cao, D., Zhang, Y., Ma, J., Qi, J., Wang, Q., Lu, G., Wu, Y., Yan, J., Shi, Y., et al. (2017). Cryo-EM structures of MERS-CoV and SARS-CoV spike glycoproteins reveal the dynamic receptor binding domains. Nat. Commun. *8*, 15092.

Yurkovetskiy, L., Wang, X., Pascal, K.E., Tomkins-Tinch, C., Nyalile, T.P., Wang, Y., Baum, A., Diehl, W.E., Dauphin, A., Carbone, C., et al. (2020). Structural and functional analysis of the D614G SARS-CoV-2 spike protein variant. Cell *183*, 739–751.e8.

Zhou, P., Yang, X.-L., Wang, X.-G., Hu, B., Zhang, L., Zhang, W., Si, H.-R., Zhu, Y., Li, B., Huang, C.-L., et al. (2020). A pneumonia outbreak associated with a new coronavirus of probable bat origin. Nature *579*, 270–273.

Zhou, P., Yuan, M., Song, G., Beutler, N., Shaabani, N., Huang, D., He, W., Zhu, X., Callaghan, S., Yong, P., et al. (2021). A protective broadly cross-reactive human antibody defines a conserved site of vulnerability on beta-coronavirus spikes. BioRxiv. https://doi.org/10.1101/2021.03.30.437769.

Zivanov, J., Nakane, T., Forsberg, B.O., Kimanius, D., Hagen, W.J., Lindahl, E., and Scheres, S.H. (2018). New tools for automated high-resolution cryo-EM structure determination in RELION-3. ELife *7*, e42166.

Zost, S.J., Gilchuk, P., Case, J.B., Binshtein, E., Chen, R.E., Nkolola, J.P., Schäfer, A., Reidy, J.X., Trivette, A., Nargi, R.S., et al. (2020a). Potently neutralizing and protective human antibodies against SARS-CoV-2. Nature *584*, 443–449.

Zost, S.J., Gilchuk, P., Chen, R.E., Case, J.B., Reidy, J.X., Trivette, A., Nargi, R.S., Sutton, R.E., Suryadevara, N., Chen, E.C., et al. (2020b). Rapid isolation and profiling of a diverse panel of human monoclonal antibodies targeting the SARS-CoV-2 spike protein. Nat. Med. *26*, 1422–1427.

STAR★METHODS

KEY RESOURCES TABLE

REAGENT or RESOURCE	SOURCE	IDENTIFIER
Antibodies		
Mouse anti-nucleocapsid	Dr. Thomas Moran, CTAD, Icahn School of Medicine	N/A
Goat anti-mouse AlexaFluor 647	Abcam	Cat#Ab150115; RRID:AB_2687948
Goat sulfo-tag anti-human antibody	Meso Scale Discovery (MSD)	Cat#R32A
Human IgG	Sigma-Aldrich	Cat#I4506; RRID:AB_1163606
Human IgG1 Fc	R & D Systems	Cat#110-HG; RRID:AB_276244
Bacterial and virus strains		
SARS-CoV-2 wild type	CDC	https://www.cdc.gov/coronavirus/2019-ncov/lab/grows-virus-cell-culture.html
SARS-CoV-2 B.1.1.7	CDC	https://www.cdc.gov/coronavirus/2019-ncov/lab/grows-virus-cell-culture.html
SARS-CoV-2 B.1.351	CDC	https://www.cdc.gov/coronavirus/2019-ncov/lab/grows-virus-cell-culture.html
SARS-CoV-2 pseudoviruses	Robbiani, et al. 2020	This paper
Chemicals, peptides, and recombinant proteins		
Recombinant SARS-CoV-2 S2	SinoBiological	Cat#40590-V08H
Recombinant SARS-CoV-2 S1	SinoBiological	Cat#40591-V08H
3XFLAG peptide	Sigma-Aldrich	Cat#SAE0194
Spike Extracellular Domain (ECD) 1-1208	ImmunityBio, Inc.	In-house production
F-octylmaltoside solution	Anatrace	Cat#O310F
Cardiolipin	Sigma-Aldrich	Cat#C0563
Keyhole limpet hemocyanin (KLH)	Sigma-Aldrich	Cat#H8283
Lipopolysaccharide (LPS)	InVivoGen	Cat#tlrl-eblps
SsDNA	Sigma-Aldrich	Cat#D8899
DsDNA	Sigma-Aldrich	Cat#D4522
Insulin	Sigma-Aldrich	Cat#I9278
Critical commercial assays		
Nano-Glo Luciferase Assay System	Promega	Cat#N1531
Deposited data		
N017 cryoEM	This paper	PDB D_1000259347
N-612-056 RBD Xray	This paper	PDB D_1000259346
N004 S1 cryoEM	This paper	PDB D_1000259349
Experimental models: Cell lines		
Chinese Hamster Ovary S (CHO-S) cells	Gibco	Cat#A11557-01
Human Embryonic Kidney (HEK) 293T cells	ATCC	Cat#CRL-3216
ACE2-Expressing HEK 293T cells	Robbiani et al. 2020	This paper
Vero E6 cells	ATCC	Cat#CRL-1586
Software and algorithms		
Prism 8	GraphPad, Inc.	https://www.graphpad.com/guides/prism/8/user-guide/new-organization.htm
Octet Data Analysis HT 10.0	Sartorius Corp.	https://www.sartorius.com/en/products/protein-analysis/octet-systems-software
cryoSPARCv3.1	Punjani et al., 2017	
SerialEM automated data collection	Mastronarde, 2005	

(*Continued on next page*)

Continued

REAGENT or RESOURCE	SOURCE	IDENTIFIER
Relion v3.1	Zivanov et al., 2018	
XDS	Kabsch, 2010	
AIMLESS	Winn et al., 2011	
PHASER	McCoy et al., 2007	
PHENIX v1.19	Adams et al., 2010	
Coot v0.9.3	Emsley et al., 2010	
PDBePISA	Krissinel and Hanrick, 2007	
Other		
T7 run-off transcription	Thermo Fisher	Cat#AM1334
pF30P linker	Liu et al., 2000	
T4 DNA ligase	New England Biolabs (NEB)	Cat#M0202
M2 anti-FLAG beads	Sigma-Alrich	Cat#A2220
Super Script II	Thermo Fisher	Cat#18064014
Streptavidin M280 Dynabeads	Thermo Fisher	Cat#11205D
Oligo(dT)25 Dynabeads	Thermo Fisher	Cat#61002
PURExpress	NEB	Cat#E6800
PURExpress Disulfide Bond Enhancer	NEB	Cat#E6820
KOD Hot Start Polymerase	EMD	Cat#71086
Gene Block	IDT	Custom; this paper
pcDNA.3 vector	Thermo Fisher	Cat#V79202
pEAK8 vector	Edge Bio	N/A
NEBuilder Hifi DNA Assembly Master Mix	NEB	Cat#E2621L
FectoPRO/PolyPlus-Transfection (transient)	Polyplus	Cat#101000007
CD-CHO media	Gibco/Thermo Fisher	Cat#10743029
Lipofectamine 2000 (transient transfection)	Thermo Fisher	Cat#11668019
OC-400 processing assemblies	Maxcyte	Cat#SOC4
Efficient Feed A	Thermo Fisher	Cat#A1023401
FunctionMax Titer Enhancer	Thermo Fisher	Cat#1501001
HiTrap MabSelect SuRe column	GE Health Care Life Sciences	Cat#11003494
HiTrap Protein L column	GE Health Care Life Sciences	Cat#29048665
Superdex 200 10/300 GL column	GE Health Care Life Sciences	Cat#17517501
Ni-NTA resin	Qiagen	Cat#30230
Anti-hIgG Fc Capture biosensors	Sartorius Corp.	Cat#18-5063
Anti-Penta-His biosensors	Sartorius Corp.	Cat#19-5120
Ni-NTA biosensors	Sartorius Corp.	Cat#18-5101
High Precision Streptavidin biosensors	Sartorius Corp.	Cat#18-5117
Luciferase Cell Culture Lysis reagent	Promega	Cat#E1531
QuantFoil grid	EM Sciences	Cat#Q225CR-06
Superdex 200 10/300 column	Cytiva	Cat#28-9909-44
Crystallization screens	Hampton Research	multiple
Sepax Proteomix HIC butyl-NP5 column	Sepax Tech	Cat#431NP2
Zenix-C SEC-300 column	Sepax Tech	Cat#233300
SYPRO orange	Thermo Fisher	Cat#S6650

RESOURCE AVAILABILITY

Lead contact

Further information and requests for resources and reagents should be directed to and will be fulfilled by C. Anders Olson (anders.olson@immunitybio.com).

Materials availability

All expression plasmids generated in this study for CoV proteins, CoV pseudoviruses, human Fabs and IgGs are available upon request through a Materials Transfer Agreement (MTA).

Data and code availability

Data availability: All data supporting the findings of this study are found within the paper and its supplemental information. The atomic model generated for the N-612-056 Fab complexed with SARS-CoV-2 RBD have been deposited in the Protein DataBank (PDB, http://www.rcsb.org/) under accession code PDB:7S0B. The atomic models and cryo-EM maps generated for the N-612-017, N-612-014, and N-612-004 Fabs complexed with SARS-CoV-2 S have been deposited at the PDB (http://www.rcsb.org/) and the Electron Microscopy Databank (EMDB) (http://www.emdataresource.org/) under accession codes PDB: 7S0C, 7S0D, 7S0E and EMDB: EMD-24786, EMD-24787, EMD-24788, respectively. All models and maps are publicly available as of the date of publication.

Code availability: This paper does not report original code.

Any additional information required to reanalyze the data reported in this paper is available from the lead contact author upon request.

EXPERIMENTAL MODEL AND SUBJECT DETAILS

CHO-S cells: Suspended CHO-S (female) cells (Gibco; Cat#A11557-01) are grown in CD-CHO media supplemented with 8 mM L-glutamine in shaker flasks at 37°C with 125 rpm rotation and 8% CO_2. CHO-S cells are propagated by seeding at a density of 1×10^6 cells/mL in new culture flasks.

HEK 293T cells: HEK 293T (female) cells (ATCC Cat#CRL-3216) are grown in DMEM (Gibco Cat# 11,995-065) with 10% heat inactivated FBS (Sigma-Aldrich) and 1X PSA (100 units/mL penicillin, 100 μg/mL streptomycin, 0.25 ug/mL Amphotericin B; all Sigma-Aldrich) at 37°C and 5% CO_2. HEK 293T cells for pseudovirus generation were cultured similarly, but with 5 mg/ml Gentamicin (Sigma-Aldrich).

Vero E6 cells: Vero E6 (female) cells (ATCC; Cat # CRL-1586) are maintained in MEM containing 10% FBS at 37°C and 5% CO_2. All SARS-CoV-2 virus stocks were from the CDC.

293TACE2 cells: 293TACE2 (female) cells for pseudovirus production (Robbiani et al., 2020) are grown in DMEM (Gibco Cat# 11,995-065) with 10% FBS and 5 mg/m gentamicin (Sigma-Aldrich), and 5 mg/mL Blasticidin (GIBCO) at 37°C and 5% CO_2.

METHOD DETAILS

mRNA display

A synthetic VH3/Vk1 scFv library (Olson, 2021) was transcribed by T7 run-off transcription (ThermoFisher; Cat #AM1334), followed by ligation to the pF30P linker (Liu et al., 2000) via a splint oligonucleotide by T4 DNA ligase (New England Biolabs, NEB; Cat #M0202). After lambda exonuclease digestion to remove splint and unincorporated linker, the ligated mRNA was purified by oligo $(dT)_{25}$ dynabeads (ThermoFisher; Cat #61002). The mRNA-puromycin template was translated (PURExpress, NEB; Cat #E6800 and #E6820) followed by incubation with KCl (550 mM final) and $MgCl_2$ (60 mM final) for 1 h at room temperature to enhance fusion formation (Liu et al., 2000). The mRNA-scFv fusions were then affinity-purified using M2 anti-Flag beads (Sigma-Aldrich; Cat #A2220) to remove non-fused template and sequences containing nonsense mutations (Liao et al., 2009; Olson et al., 2011). After elution with 3XFlag peptide (Sigma-Aldrich; Cat #SAE0194), the fusions were reverse transcribed with Super Script II (ThermoFisher; Cat #18064014). The pool was incubated with biotinylated SARS CoV2 Spike extracellular domain bound to 5 μL streptavidin M280 Dynabeads (ThermoFisher; Cat #11205D) for 1 h at room temperature. After washing, the immobilized fusion samples were eluted by heat (95°C) and PCR amplified with KOD hot start polymerase (EMD; Cat #71086). Affinity maturation was performed by replacing the wild type CDRs H1, H2, H3, and L3 with synthetic DNA cassettes derived from oligonucleotides doped at 6% (Hutchison et al., 1986) and performing 3–5 rounds of mRNA display as described above.

Production antibodies and recombinant SARS-CoV-2 S domains

Molecular cloning

SARS-CoV-2 Spike ECD 1–1208 (682-GSAS-685; 986-PP-987; synthesized in-house) fused to the T4 fibritin trimerization domain with C-terminal Avi- and His-tag were synthesized with gene block (IDT; custom) and cloned into pcDNA.3 vector. RBD-SD1, wild type RBD and mutant RBD domains were subcloned into pcDNA.3 vector with C-terminal His-tag.

VH and VL sequences of candidate sequences were cloned into a pEAK8 based vector (Edge Bio) with dual CMV promotor harboring IgG1 heavy chain and light chain backbone using NEBuilder Hifi DNA Assembly Master Mix (NEB; Cat #E261L).

FectoPRO® transient transfection of antibodies

For transient expression of antibodies by FectoPRO® transfection (Polyplus: Cat #101000007), CHO-S cells in suspension were cultured in CD-CHO media supplemented with 8 mM L-glutamine in shaker flasks at 37°C with 125 rpm rotation and 8% CO_2. One day before transfection, CHO-S cells were seeded at a density of 1×10^6 cells/mL in 45 mL culture flask. On the day of transfection, 75 μL of FectoPRO® transfection reagent was mixed with 5 mL of 15 μg/mL pcDNA3 plasmid DNA (ThermoFisher: Cat #V79202) harboring

antibody encoding sequence in CD-CHO media and incubated for 10 min at room temperature. The DNA/transfection reagent mixture was added to 45 mL of CHO-S culture and incubated at 37°C with 5% CO_2 and 125 rpm rotation. On Day 3, 50 mL of the CD-CHO media (Gibco; Cat # 10,743,029) supplemented with 8 mM L-glutamine was added and the culture incubated for an additional 4 days.

Lipofectamine® transient transfection of RBD constructs

For transient expression of RBD-SD1, RBD wild-type and RBD mutants, 293T cells were cultured and incubated at at 37°C with 5% CO_2. Plasmid harboring RBD constructs were mixed with Lipofectamine 2000 (ThermoFisher; Cat #11668019) with 1:1 (v:v) ratio and incubated for 20 min at room temperature. The mixture was then added to the culture and incubated for 3–4 days.

Maxcyte® transient transfection of SARS-CoV-2-S ECD trimer

For transient expression of SARS-CoV-2 S di-Pro ECD timer by Maxcyte® transfection (ExPERT ATx), CHO-S cells were cultured in suspension in CD-CHO media supplemented with 8 mM L-glutamine in shaker flasks at 37°C with 125 rpm rotation and 8% CO_2. For transfection, cells in the exponential growth stage were pelleted by centrifugation at 1,400 rpm for 10 min, re-suspended in 10 mL of electroporation buffer, and re-pelleted at 1,400 rpm for 5 min. The cell pellet was resuspended at a density of 2×10^8 cells/mL in electroporation buffer, mixed with the plasmid harboring SARS-CoV-2 S di-Pro ECD sequence at a concentration of 150 μg/mL, and transfected using OC-400 processing assemblies in a Maxcyte® ExPERT ATx Transfection System. Transfected cells were incubated for 30 min at 37°C, 5% CO_2 and then resuspended in Efficient Feed A Cocktail - CHO-CD EfficientFeed™ A (ThermoFisher; Cat #A1023401) + 0.2% Pluronic F-68 + 1% HT Supplement +1% L-glutamine - at a density of ~4-6 x 10^6 cells/mL. This cell culture was incubated at 37°C with 5% CO_2 and 125 rpm rotation overnight, 1 mM Na butyrate was added, and the culture was further incubated at 32°C with 3% CO_2 and 125 rpm for 13 more days; during this incubation period, Maxcyte® Feed Cocktail - 13.9% CD Hydrolysate, 69.5% CHO CD EfficientFeed™ A, 6.2% Glucose, 6.9% FunctionMax™ Titer Enhancer, 3.5% L-Glutamine - was added at 10% of the culture volume on Days 3 and Day 8.

Purification of IgGs

FectoPRO® transfection cell culture medium was centrifuged and filtered through a 0.22 μm filter to remove cells and debris, then loaded onto a HiTrap™ MabSelect SuRe™ column (GE Healthcare Life Sciences; Cat #11003494) on the AKTA Pure system (Cytiva) pre-equilibrated with 10 mM $NaPO_4$ and 150 mM NaCl at pH 7.0. After loading, the column was washed with 10 column volumes of the same buffer. The protein was eluted with 100 mM NaOAc, pH 3.6, then immediately neutralized using 2 M Tris pH 8.0. The elution fractions were pooled and dialyzed into 10 mM Hepes and 150 mM NaCl at pH 7.4.

Purification of Fabs

Fabs were generated by papain digestion using crystallized papain (Sigma-Aldrich; Cat #1495005) in 50 mM $NaPO_4$, 2 mM EDTA, 10 mM L-cysteine, pH 7.4 for 30–60 min at 37°C at a 1:100 enzyme:IgG ratio. Fab and partially cleaved IgG were applied on 1-mL HiTrap Protein L column (GE Healthcare Life Science; Cat #29048665). After loading, the column was washed with 10 column volumes of 10 mM $NaPO_4$ and 150 mM NaCl at pH 7.0. The protein was eluted with 100 mM Na citrate, pH 2.5, then immediately neutralized using 2 M Tris pH 8.0. The elution fractions were pooled and dialyzed into 10 mM Hepes and 150 mM NaCl at pH 7.4. Fabs were further purified by SEC using a Superdex 200 10/300 GL column (GE Healthcare Life Sciences; Cat #17517501) in 10 mM Hepes and 150 mM NaCl at pH 7.4.

Purification of di-pro S timer, RBD-SD1, RBD wild-type, and RBD mutants

The Lipofectamine transfection cell culture medium and Maxcyte transfection cell culture medium was centrifuged and filtered through a 0.22 μm filter or 0.45 μm, respectively, to remove cells and debris. Then, 50 mM Tris, 100 mM NaCl, and 10 mM imidazole was added to the supernatant before loading to a gravity column packed with Ni-NTA resins (Qiagen; Cat #30230) pre-equilibrated with 20 mM Tris, 300 mM NaCl, and 10 mM imidazole, pH 8.0. After loading, the column was washed with 10 column volumes of the same buffer. The protein was eluted with 20 mM Tris, 150 mM NaCl, and 300 mM imidazole. The elution fractions were pooled and dialyzed into 10 mM Hepes and 150 mM NaCl, pH 7.4.

Bio-layer interferometry (BLI) kinetic analysis of antibodies

BLI buffer used in all experiments was 10 mM Hepes, 150 mM NaCl, pH 7.4, with 0.02% Tween 20, and 0.1% BSA. Analytes used in kinetic analysis were uncleavable S trimer, RBD-SD1, RBD wild-type, RBD mutants, commercially purchased recombinant SARS-CoV-2 S2 and SARS-CoV-2 S1 (SinoBiological; Cat #s 40,590- and 40,591-V08H, respectively). For determining binding affinities, IgGs were immobilized on Anti-hIgG Fc Capture (AHC) biosensors (Sartorius; Cat # 18–5063) and a concentration series of 200, 100, 50, 25, 12.5, 6.25, 3.125 nM was used to determine the equilibrium dissociation constants (K_D values) for RBD-SD1, RBD wild-type, RBD mutants, and S1 using 1:1 binding curve fit. For some RBD mutants that weakened binding and showed biphasic dissociation, only 30 s dissociation curves were used to fit 1:1 binding model. A concentration series of 20, 10, 5, 2.5, 1.25, 3.13, 1.56 nM was used to determine apparent K_D for uncleavable S trimer using bivalent model on Octet HT software. For determining 1:1 binding affinity for S2, S2-His-tag was immobilized on Anti-Penta-His (HIS1K) biosensors (Sartorius; Cat #18–5120), and a concentration series of S2 binding mAb Fab at 200, 100, 50, 25, 12.5, 6.25, 3.125 nM was used.

ACE2 blocking assay

RBD-His-tag at 5 μg/mL was first loaded on Ni-NTA (NTA) biosensors (Sartorius; Cat #18–5101) for 15 s and subsequently blocked with 5 μg/mL mAbs or BLI assay buffer for 5 min. BLI signal from ACE2 binding were measured by incubating RBD-coated/mAb blocked biosensors in 25 nM ACE2-IgG1Fc for 3 min.

Epitope binning

For epitope binning using S1 domain, biotinylated S1 binding mAbs at 25 μg/mL were first loaded on High Precision Streptavidin SAX biosensors (Sartorius; Cat #18–5117) for 10 s 3.75 μg/mL of recombinant SARS-CoV-2 S1 were used to bind mAb captured on biosensors for 3 min and subsequently 10 μg/mL S1 binding mAb were incubated with biosensors to observe binding competition and signal was recorded for 3 min. For epitope binning using S2 domain, recombinant SARS-CoV-2 S2-His-tag at 10 μg/mL was loaded on Anti-Penta-HIS biosensors for 1 min 10 μg/mL of S2 binding mAbs were sequentially incubated with biosensors for 3-5 min to observe binding competition.

Developability assays

Meso scale diagnostics (MSD) polyreactivity

Six different antigens, cardiolipin at 50 μg/mL (Sigma-Aldrich; Cat #C0563), keyhole limpet hemocyanin (KLH) at 5 μg/mL (Sigma-Aldrich; Cat #H8283), lipopolysaccharide (LPS) at 10 μg/mL (InVivoGen; tlrl-eblps), ssDNA at 1 μg/mL (Sigma-Aldrich; Cat #D8899), dsDNA at 1 μg/mL (Sigma-Aldrich; Cat #D4522), and insulin at 5 μg/mL (Sigma-Alrich; Cat #I9278) were coated onto Meso Scale Discovery (MSD) MULTI-Array 96-well plate (MSD) individually at 50 μL per well overnight at 4°C. Plates were blocked with PBS with 0.5% BSA at room temperature for 1 h, followed by three washes with PBST (PBS plus 0.05% Tween 20). Fifty microliters of 100 nM testing antibody solution were added to each well and incubated at RT for 1 h followed by six washes with 100 μL of PBS. Twenty microliters of 0.25 μg/mL SULFO-tag, anti-Human antibody (MSD; Cat #R32A) were added to the wells and incubated for 1 h followed by six washes as before. Finally, 150 μL of 2X MSD Read Buffer T (MSD) was added to each well, and electrochemilluminescence signal was read by MSD Sector Imager. Polyreactivity score was determined by normalizing signal by control wells with no test antibody.

Hydrophobic interaction column (HIC)

Five (5) μg antibody samples (1 mg/mL) were spiked in with a mobile phase A solution (1.8 M ammonium sulfate and 0.1 M sodium phosphate at pH 6.5) to achieve a final ammonium sulfate concentration of about 1 M before analysis. A Sepax Proteomix HIC butyl-NP5 column (Sepax Tech; Cat #431NP2) on Agilent 1100 HPLC was used with a liner gradient of mobile phase A and mobile phase B solution (0.1 M sodium phosphate, pH 6.5) over 20 min at a flow rate of 1 mL/min with UV absorbance monitoring at 280 nm. Elution time was recorded.

Clone self-interaction by bio-layer interferometry (CSI-BLI)

Human IgG (Sigma-Aldrich; Cat #I4506) was loaded to an AHQ biosensor (ForteBio) to ~1 nm, followed by sensor blocking with human IgG1 Fc (R&D Systems; Cat #110-HG). The self-association was performed at 1 μM solution concentration of antibodies for 300s on an Octet Red96e system (Sartorius Corporation). The binding response from the association step was subtracted from that of a reference IgG.

Accelerated stability assay

Antibody samples at 1 mg/mL were kept at 40°C for 30 days in 10 mM Hepes and 150 mM sodium chloride, pH 7.4. 10 μg of antibody was loaded onto Zenix-C SEC-300 size-exclusion column (Sepax Tech; Cat #233300) on HPLC at Day 0, 5, 20, and 30. A long-term stability slope (% aggregation/day) was calculated from the percent aggregated measured on the SEC-HPLC at each time point.

Differential scanning fluorimetry (DSF) analysis of melting temperature (Tm)

Twenty (20) mLicroliters of 1 mg/mL antibody sample were mixed with 10 μL of 20x SYPRO Orange (ThermoFisher; Cat #S6650) in a 96-well PCR plate (ThermoFisher). The plate was scanned from 40°C to 95°C at a rate of 0.5°C/ 2 min in a CFX96 Real-Time PCR system (Bio-Rad). The Fab Tm was assigned using the first derivative of the raw data. Tm of each Fab is interpolated from the largest dF/dT peak of the melting curves resulting from the combination of CH2, CH3, and Fab melting.

Convalescent plasma blocking assay

Spike trimer with C-terminal biotin at 5 μg/mL was first loaded on High Precision Streptavidin SAX biosensors (Sartorius) for 75 min. Spike coated biosensor was subsequently blocked with 10-fold diluted SARS-CoV-2 convalescent plasma for 15 min. BLI signal from 10 mAbs binding to available surface of spike timer were measure by incubating Spike-coated/plasma blocked biosensors in 10 μg/mL of mAbs for 3 min. BLI signal was compared to self-blocking of N-612-017/N-612-017 and non-blocking pair of N-612-017/N-612-004 to determine whether each mAb was completely blocked, partially blocked, or non-blocked by convalescent plasma from 4 different patients.

Vero E6 neutralization assay

All aspects of the assay utilizing virus were performed in a BSL3 containment facility according to the ISMMS Conventional Biocontainment Facility SOPs for SARS-CoV-2 cell culture studies. Vero E6 cells (ATCC; Cat # CRL-1586) were seeded into 96-well plates at 20,000 cells/well and cultured overnight at 37°C. The next day, 3-fold serial dilutions of mAbs were prepared in DMEM containing 2% FBS, 1% NEAAs, and 1% Pen-Strep (vDMEM). SARS-CoV-2 virus stock (CDC) was prepared in vDMEM at 10,000 TCID50/mL, mixed 1:1 (v:v) with the mAb dilutions, and incubated for 30 min or 24 h at 37°C. Media was removed from the Vero E6 cells, mAb-virus complexes were added and incubated at 37°C for 48 h. Cells were fixed with 4% paraformaldehyde (PFA) in the BSL3 facility for 24 h before being taken out for further processing. Cells were briefly washed with PBS and permeabilized with 0.1% Triton-X 100 for 15 min. After three washes with PBS, cells were blocked at room temperature for 1 h using PBS containing 0.5% FBS, then

incubated with in-house (from Dr. Thomas Moran) anti-SARS-CoV-2 nucleocapsid protein (NP) mouse serum at 1:2000 dilution overnight at 4°C. After three washes of PBS, cells were incubated with goat anti-mouse Alexa Fluor® 647 (Abcam; Cat #ab150115) at a 1:2000 dilution. Cell nuclei were stained using DAPI (1:20,000 dilution). Control wells including six wells on each plate for no virus and virus-only controls were used. The percent neutralization was calculated as 100 − ((sample of interest − [average of "no virus"])/[average of "virus only"]) * 100) using images of wells containing Np-labeled cells collected by a Celigo Imaging Cytometer (Nexcelom Bioscience).

Pseudovirus neutralization assays

Pseudoviruses based on HIV lentiviral particles were prepared as described (Robbiani et al., 2020). Three-fold serially diluted mAbs were incubated with SARS-CoV-2 pseudovirus for 1 h at 37°C. After incubation with 293TACE2 cells for 48 h at 37°C, cells were washed twice with PBS, lysed with Luciferase Cell Culture Lysis 5X reagent (Promega; Cat #E1531), and NanoLuc Luciferase activity in lysates was measured using the Nano-Glo Luciferase Assay System (Promega; Cat #N1531). Relative luminescence units (RLUs) were normalized to values derived from cells infected with pseudovirus in the absence of mAbs. Half-maximal inhibitory concentrations (IC_{50} values) for mAbs were determined using 4-parameter nonlinear regression (Prism, GraphPad).

Cryo-EM sample preparation

N-612-004, N-612-014 and N-612-017 Fab-S complexes were assembled by incubating purified SARS-CoV-2 S trimer at a 1.1:1 molar excess of purified Fab per S protomer at RT for 20 min. Complex was mixed with F-octylmaltoside solution (Anatrace; Cat #0310F) to a final concentration of 0.02% w/v and then 3 μL were immediately applied to a 300 mesh, 1.2/1.3 QuantiFoil grid (EM Sciences; Cat # #Q225CR-06) that had been freshly glow discharged for 30s at 20 mA using a PELCO easiGLOW (Ted Pella). The grid was blotted for 3s with Whatman No. 1 filter paper at 22°C and 100% humidity then vitrified in 100% liquid ethane using a Mark IV Vitrobot (FEI) and stored under liquid nitrogen.

Cryo-EM structure determination of N-612-004, N-612-014, and N-612-017 Fab in complex with S-6P

Single-particle cryo-EM data were collected for Fab-S trimer complexes as previously described (Barnes et al., 2020b) Briefly, movies were collected on a 200 kV Talos Arctica transmission electron microscope (ThermoFisher) equipped with a Gatan K3 Summit direct electron detector operating in counting mode. Movies were collected using a 3 × 3 beam image shift pattern with SerialEM automated data collection software (Mastronarde, 2005) at a nominal magnification of 450,00x (super-resolution 0.4345 Å/pixel) using a defocus range of −0.7 to −2.0 μm. An average dose rate of 13.5 e^-/pix/s resulted in a total dose of ~60 e−/$Å^2$ over 40 frames for all datasets.

For all datasets, movies were patch motion corrected for beam-induced motion including dose-weighting within cryoSPARC v3.1 (Punjani et al., 2017) after binning super resolution movies by 2 (0.869 Å/pixel). The non-dose-weighted images were used to estimate CTF parameters using Patch CTF in cryoSPARC, and micrographs with poor CTF fits, signs of crystalline ice, and field of views that were majority carbon were discarded. Particles were picked in a reference-free manner using Gaussian blob picker in cryoSPARC (Punjani et al., 2017) Initial particle stacks were extracted, binned x4 (3.48 Å/pixel), and subjected to *ab initio* volume generation (4 classes) and subsequent heterogeneous refinement with all particles. The 3D classes that showed features for a Fab-S trimer complex or Fab-S1 protomer were 2D classified to polish particle stacks. The resulting particle stacks were unbinned (0.869 Å/pixel) and re-extracted using a 432 box size, and moved to Relion v3.1 (Zivanov et al., 2018) for further 3D classification. Particles corresponding to distinct states were separately refined using non-uniform 3D refinement imposing C1 symmetry in cryoSPARC and final resolutions were estimated according to the gold-standard FSC (Bell et al., 2016).

To improve features at the Fab-RBD interface, focused, non-uniform 3D local refinement in cryoSPARC were performed by applying a soft mask around the Fab V_HV_L – RBD (N-612-017), NTD (N-612-014), or SD1 (N-612-004) domains. These efforts resulted in a modest improvement in the Fab-S interface, which helped accurate model building.

X-Ray crystallography structure determination of N-612-056 in complex with RBD

The N-612-056-RBD complex was assembled by incubating the SARS-CoV-2 RBD with a 2x molar excess of Fab for 1 h on ice followed by size exclusion chromatography on an superdex200 10/300 increase column (Cytiva; Cat # 28-9909-44). Fractions containing complex were pooled and concentrated to 5–8 mg/mL. Crystallization trials using commercially-available screens (Hampton Research) were performed at room temperature using the sitting drop vapor diffusion method by mixing equal volumes of the Fab-RBD complex and reservoir using a TTP LabTech Mosquito instrument. Crystals were obtained for N-612-056-RBD complex in 0.2 M Lithium citrate tribasic tetrahydrate and 20% w/v polyethylene glycol 3,350, subsequently cryoprotected by adding glycerol directly to drops to a final concentration of 20% v/v and cryopreserved in liquid nitrogen.

X-ray diffraction data were collected at the Stanford Synchrotron Radiation Lightsource (SSRL) beamline 12-2 on a Pilatus 6M pixel detector (Dectris). Data from single crystals were indexed and integrated in XDS (Kabsch, 2010) and merged using AIMLESS in *CCP4* (Winn et al., 2011) (Table S6 supplemental information). The N-612-056-RBD structure was solved by molecular replacement in PHASER (McCoy et al., 2007) using unmodified RBD coordinates (PDB: 7K8M) and coordinates from C002 Fab (PDB: 7K8O) as search models, after removal of C002 heavy chain and light chain CDR loops. Coordinates were rigid body and B-factor refined in PHENIX v1.19 (Adams et al., 2010) followed by sequence matching and repeated cycles of *phenix.refine* and manual building in Coot (v0.9.3) (Emsley et al., 2010) (Table S6 supplemental information).

Structure analyses

Buried surface area estimates were made using PDBePISA with a 1.4Å probe (Krissinel and Henrick, 2007). Potential hydrogen bonds were assigned using a distance of <3.6Å (Krissinel and Henrick, 2007) and an A-D-H angle of >90°C, and the maximum distance allowed for a van der Waals interaction was 4.0 Å. Structure figures were made using UCSF Chimera v1.14 (Goddard et al., 2018).

QUANTIFICATION AND STATISTICAL ANALYSIS

All software used for structural analysis and processing is listed in the Key Resources table. The half-maximal inhibitory concentrations for monoclonal antibodies (IC50s) reported in Figures 2 and 7 were determined by plotting % neutralization calculated by 100 − ((sample of interest − [average of "no virus"])/[average of "virus only"]) * 100) using images of wells containing Np-labeled cells followed by 4-parameter nonlinear regressions analyzed using GraphPad Prism. IC50s reported in Figure 6 were determined by normalizing relative luminescence units (RLUs) to values derived from cells infected with SARS-CoV-2 pseudovirus in the absence of antibodies followed by a 4-parameter nonlinear regression (least-squares regression method without weighting) using GraphPad Prism. Numbers of replicates and experiments are indicated in the respective figure legends.

Cell Reports, Volume *38*

Supplemental information

Rapid identification of neutralizing antibodies against SARS-CoV-2 variants by mRNA display

Shiho Tanaka, C. Anders Olson, Christopher O. Barnes, Wendy Higashide, Marcos Gonzalez, Justin Taft, Ashley Richardson, Marta Martin-Fernandez, Dusan Bogunovic, Priyanthi N.P. Gnanapragasam, Pamela J. Bjorkman, Patricia Spilman, Kayvan Niazi, Shahrooz Rabizadeh, and Patrick Soon-Shiong

Supplemental Information

Rapid Identification of Neutralizing Antibodies against SARS-CoV-2 Variants by mRNA Display

Shiho Tanaka, C. Anders Olson, Christopher O. Barnes, Wendy Higashide, Marcos Gonzalez, Justin Taft, Ashley Richardson, Marta Martin-Fernandez, Dusan Bogunovic, Priyanthi N.P. Gnanapragasam, Pamela J. Bjorkman, Patricia Spilman, Kayvan Niazi, Shahrooz Rabizadeh, Patrick Soon-Shiong

Supplemental Information

Supplementary Tables

Table S1. Ten spike binding VH/VL sequences identified by mRNA display (related to Fig. 1 and mRNA display method).

Ab	CDRH1 (26-35)	CDRH2 (50-58)	CDRH3 (93-101)	CDRL3 (89-86)	
N-612-017	GFTFSSYAMH	AIWGSGSNTY	ARGRDLAAFTKTA	QQHDALPW	
N-612-056	GFTFSSYAMS	LISGSGGSTY	ARDLWGSGFFA	QQDAGTPL	RBD binder
N-612-074	GFTFSAYAMH	AIWGSGGSTY	ARDLWMAMWFG	QQRSTYPL	
N-612-004	GFTFSSYYMH	AISGSGGYTY	ARDRDHAYDWG	QQWADWPL	SD1 binder
N-612-041	GFTFSSYTMH	AISGSGGYTY	ARDRDLLWMGWA	QQYANWPL	
N-612-002	GFTFSSYTMH	AISGSGGSTY	ARDLFDWG	QQDYGFPL	NTD binder
N-612-014	GFTFSSYAMT	YISGSGGGTY	ARDRWASGWLA	QQAYAYPL	
N-612-007	GFTFSNYAMH	AISGNGGSTG	ARDRWYVKNA	QQLDGTPF	
N-612-044	GFTFSNYAMH	AISGSGGSTY	ARDLSFWLTYHLASA	QQSYSDPL	S2 binder
N-612-086	GFTFSSYAMH	AISWSGRSTY	ARDLSSNWGSG	QQSADTPF	

Table S2. BLI kinetic parameters obtained for various SARS-CoV-2 Spike domains (RBD, RBD-SD1, S1, S2)(related to Fig. 1 and BLI kinetic analysis method).

Analyte	**nAb**	**k_{on} (1/Ms)**	**k_{off} (1/s)**	**K_D (nM)**
RBD	N-612-017	6.77E+05	3.58E-03	5.29
	N-612-056	3.37E+05	1.01E-03	2.98
	N-612-074	1.33E+05	1.48E-03	11.1
RBD-SD1	N-612-017	4.56E+05	3.94E-03	8.65
	N-612-056	3.59E+05	1.04E-03	2.89
	N-612-074	1.21E+05	3.97E-03	32.9
	N-612-004	1.51E+05	9.79E-04	6.49
	N-612-041	2.10E+05	3.35E-03	16.0
S1	N-612-017	2.77E+05	2.04E-03	7.37
	N-612-056	1.51E+05	5.86E-04	3.89
	N-612-074	1.01E+05	1.46E-03	14.4
	N-612-004	9.92E+04	2.13E-04	2.15
	N-612-041	1.25E+05	1.83E-03	14.4
	N-612-002	2.68E+05	7.26E-04	2.71
	N-612-014	1.76E+05	2.18E-03	12.4
S2 (Ligand)	N-612-007 (Fab)	3.70E+05	1.40E-03	3.79
	N-612-044 (Fab)	1.70E+05	1.61E-03	9.44
	N-612-086 (Fab)	2.67E+05	0.96E-02	11.6

Table S3. BLI kinetic parameters obtained for Spike trimer using bivalent model fit (related to Fig. 1 and BLI kinetic analysis method).

Ab	k_{on1} (1/Ms)	k_{on2} (1/Ms)	k_{off1} (1/s)	k_{off2} (1/s)	*Apparent* K_D (nM)
N-612-017	8.35E+04	1.55E+00	<1.0E-07	1.69E-02	<0.001
N-612-056	6.24E+04	1.94E+00	<1.0E-07	5.15E-02	<0.001
N-612-074	9.23E+04	8.12E-01	<1.0E-07	1.89E-01	<0.001
N-612-004	7.60E+04	4.24E+00	<1.0E-07	1.00E+00	<0.001
N-612-041	1.11E+05	4.06E-01	<1.0E-07	1.75E-01	<0.001
N-612-002	5.69E+04	6.82E-02	<1.0E-07	6.76E-02	<0.001
N-612-014	2.54E+04	3.82E-03	2.29E-07	2.82E+00	0.0033
N-612-007	5.78E+04	7.80E-02	<1.0E-07	2.92E-02	<0.001
N-612-044	7.15E+04	2.62E+00	<1.0E-07	7.14E-02	<0.001
N-612-086	6.11E+04	1.55E-01	<1.0E-07	5.53E-02	<0.001

Table S4. Developability assay summary table (related to Fig. 1 and developability assay method).

Ab	Polyreactivity MSD (Fold-over-PBS)	HIC (min)	BLI-CSI (nm)	Accelerated stability % monomer increase/day	Fab Tm (℃)
N-612-017	3	10.1	-0.06	0.09	85
N-612-056	7	11.5	0.00	0.10	74
N-612-074	31	**22.1**	-0.01	0.10	76
N-612-004	14	14.9	0.05	0.13	85
N-612-041	10	**20.4**	0.05	**0.37**	88
N-612-002	22	13.9	0.08	0.18	82
N-612-014	4	12.3	0.09	0.16	88
N-612-007	10	11.8	0.04	0.11	82
N-612-044	8	**13.4/15.4**	-0.06	0.10	88/91
N-612-086	10	13.2	0.07	0.11	88
Acceptance criteria	<50	<16	<0.2	<0.2	>65 ℃

Table S5. Cryo-EM data collection and refinement statistics (related to Figs 3 and 5).

	N-612-017 Fab SARS-CoV-2 S 6P	N-612-014 Fab SARS-CoV-2 S 6P	N-612-004 Fab SARS-CoV-2 S 6P
PDB	**7S0C**	**7S0D**	**7S0E**
EMD	**24786**	**24787**	**24788**
Data collection conditions			
Microscope	Talos Arctica	Talos Artica	Talos Arctica
Camera	Gatan K3 Summit	Gatan K3 Summit	Gatan K3 Summit
Magnification	45,000x	45,000x	45,000x
Voltage (kV)	200	200	200
Recording mode	counting	counting	counting
Dose rate (e^-/pixel/s)	13.5	13.3	13.8
Electron dose ($e^-/Å^2$)	60	60	60
Defocus range (μm)	0.7 – 2.0	0.7 – 2.0	0.7 – 2.0
Pixel size (Å)	0.8689	0.8689	0.8689
Micrographs collected	2,585	3,791	3,717
Micrographs used	2,132	3,211	2,047
Total extracted particles	282,890	505,695	595,163
Refined particles	175,986	389,223	115,068
Particles in final refinement	108,746	137,684	107,271
Symmetry imposed	C1	C1	C1
FSC 0.143 (unmasked/masked)			
unmasked	4.4 Å	6.4 Å	7.1 Å
masked	3.2 Å	3.5 Å	4.8 Å
Refinement and Validation			
Initial model used	6XKL	6XKL	6XKL
Number of atoms			
Protein	29,164	33,650	5,307
Ligand	434	873	28
MapCC (global/local)	0.81/0.78	0.79/0.76	0.87/0.69
Map sharpening B-factor	65.8	75.3	155
R.m.s. deviations			
Bond lengths (Å)	0.01	0.005	0.02
Bond angles (°)	0.9	0.89	1.5
MolProbity score	2	2.2	2.46
Clashscore (all atom)	13.4	17.7	7.9
Poor rotamers (%)	0.2	0.1	0
Ramachandran plot			
Favored (%)	94.7	93.4	92.8
Allowed (%)	5.1	6	6.3
Disallowed (%)	0.2	0.6	0.9

Table S6. X-ray crystallography data collection and refinement statistics (related to Fig. 4).

	N-612-056 - SARS2-RBD *(12-2, SSRL)*
PDB ID	**7S0B**
Data collection[a]	
Space group	$P2_12_12$
Unit cell (Å)	102.3, 153.7, 96.6
α, β, γ (°)	90, 90, 90
Wavelength (Å)	0.979
Resolution (Å)	38.9-29 (3.04-2.9)
Unique Reflections	34,420 (4,471)
Completeness (%)	99.8 (99.1)
Redundancy	6.6 (6.7)
$CC_{1/2}$ (%)	99.3 (72.8)
<I/σI>	6.4 (1.5)
Mosaicity (˚)	0.25
R_{merge} (%)	18.7 (133)
R_{pim} (%)	8.3 (59.4)
Wilson *B*-factor	56.6
Refinement and Validation	
Resolution (Å)	384 - 2.9
Number of atoms	
Protein	9,829
Ligand	28
Waters	0
R_{work}/R_{free} (%)	212/25.4
R.m.s. deviations	
Bond lengths (Å)	0.006
Bond angles (˚)	1.2
MolProbity score	2.47
Clashscore (all atom)	11.6
Poor rotamers (%)	5
Ramachandran plot	
Favored (%)	94.8
Allowed (%)	5.2
Disallowed (%)	0
Average *B*-factor (Å)	73.5

[a]Numbers in parentheses correspond to the highest resolution shell

Table S7. BLI kinetic analysis of N-612-017, N-612-017-01, N-612-017-03, N-612-017-5B02, and N-612-017-5B05 against RBD-WT, RBD-B.1.351 (K417N/E484K/N501Y) and RBD-L452R (related to Fig. 7 and BLI kinetic analysis method).

	RBD-WT			RBD-B.1.351			RBD-L452R		
	k_{on} (1/Ms)	k_{off} (1/s)	K_D (nM)	k_{on} (1/Ms)	k_{off} (1/s)	K_D (nM)	k_{on} (1/Ms)	k_{off} (1/s)	K_D (nM)
N-612-017	6.77E+05	3.58E-03	5.29	4.45E+05	1.36E-02	30.6	--	--	N.B.
N-612-017-01	5.59E+05	3.59E-04	0.64	5.31E+05	4.06E-04	0.77	2.34E+05	7.75E-03	33.1
N-612-017-03	6.48E+05	1.60E-04	0.25	6.47E+05	2.33E-04	0.36	1.18E+05	6.90E-03	58.7
N-612-017-5B02	8.24E+05	9.26E-05	0.11	7.99E+05	1.20E-04	0.15	5.74E+05	3.54E-03	6.16
N-612-017-5B05	9.62E+05	3.16E-03	3.28	9.68E+05	2.48E-03	2.56	8.01E+05	1.96E-03	2.44

Supplemental Figures

Figure S1

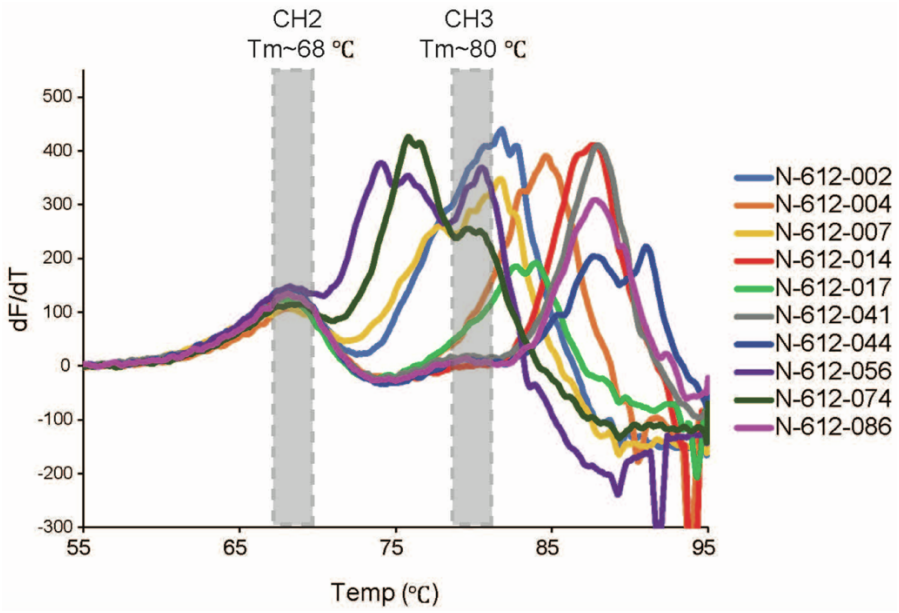

Figure S1. Tm thermograms of 10 Abs identified from mRNA library display (related to Fig. 1 and developability assay method).

Figure S2

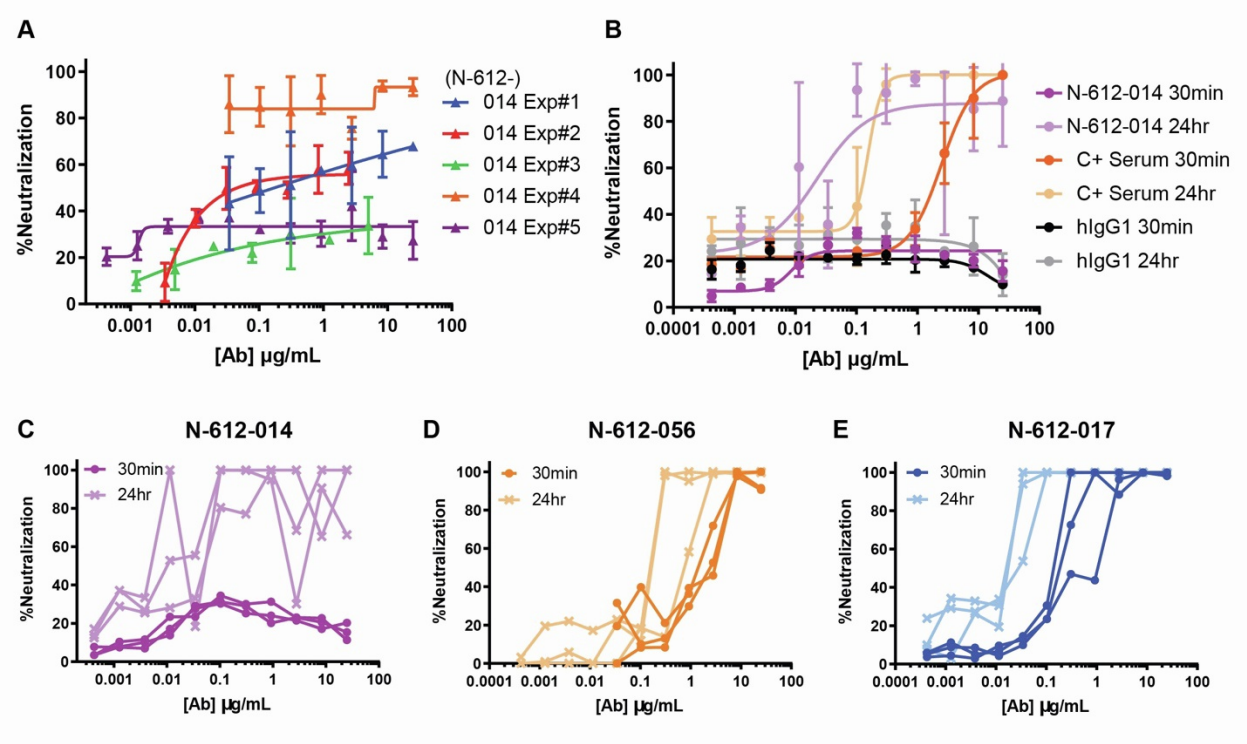

Figure S2. Vero E6 live virus neutralization assay (related to Fig. 2 and Vero E6 neutralization assay method). (A) Neutralization activity of N-612-014 in 5 separate experiments with 30 min virus-antibody incubation. (B) Comparison of neutralization activity of N-612-014 and positive control convalescent serum (C+) with 30 min. vs 24 hr virus-antibody incubation. Comparison of 30 min and 24 hr virus-antibody incubation for: (C) N-612-014, (D) N-612-056, and (E) N-612-017.

Figure S3

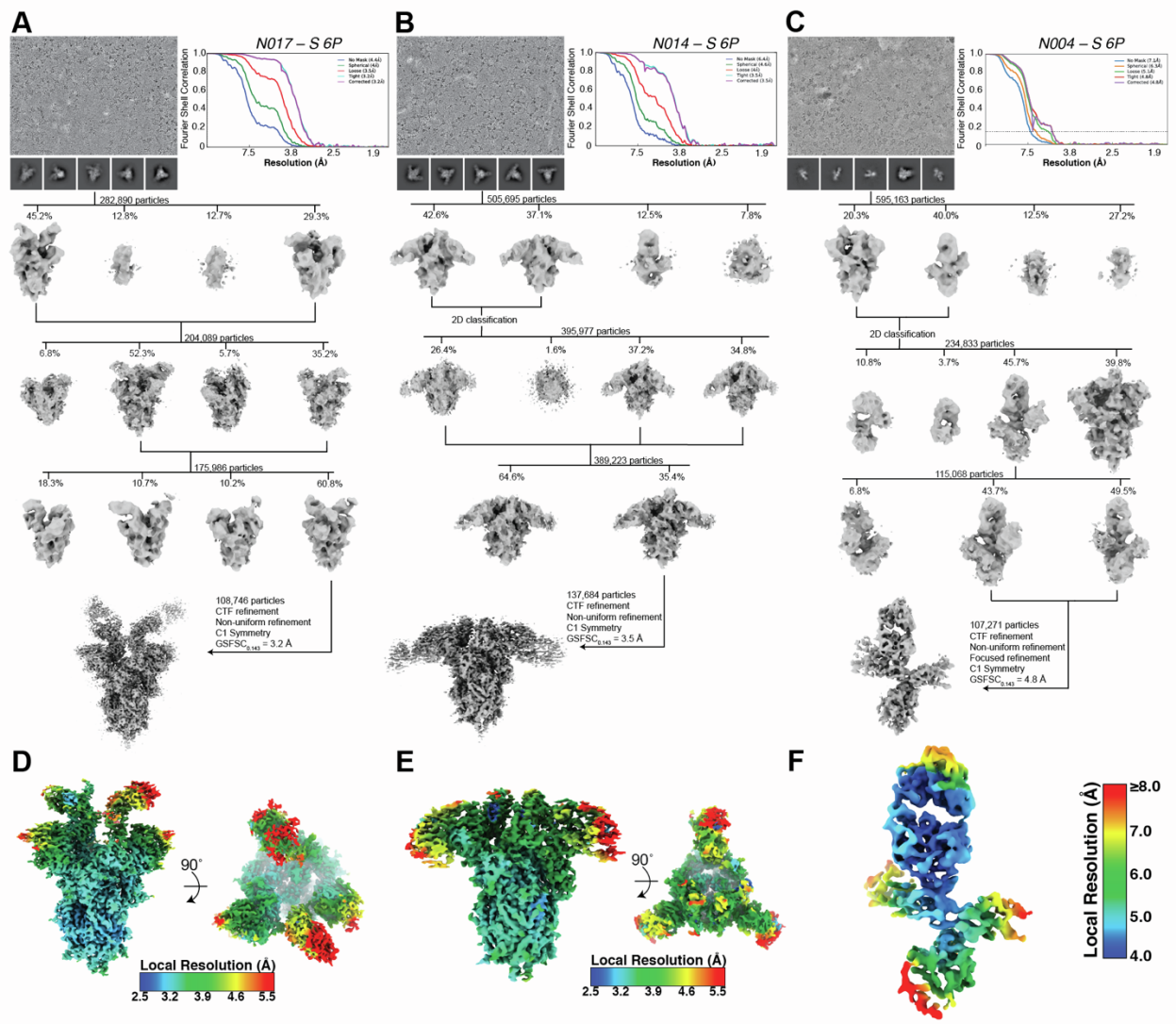

Figure S3. Cryo-EM data processing and validation (related to Figs 3 and 5). (A-C) Representative micrograph, 2D class averages, data processing workflow, and Gold Standard FSC plots for the final reconstructions of (A) N-612-017 – S 6P, (B) N-612-014 – S 6P, and (C) N-612-056 – S 6P complexes. (D-F) Local resolution estimates calculated in cryoSPARC v3.1 for (D) N-612-017 – S 6P, (E) N-612-014 – S 6P, and (F) N-612-056 – S 6P complexes.

Figure S4

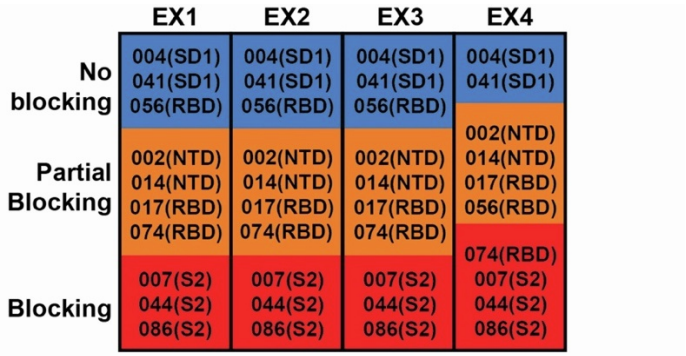

Figure S4. Convalescent plasma blocking of 10 mAbs binding to SARS-CoV-2 Spike (related to Figs 1 and 2 and convalescent plasma blocking assay method).

Figure S5

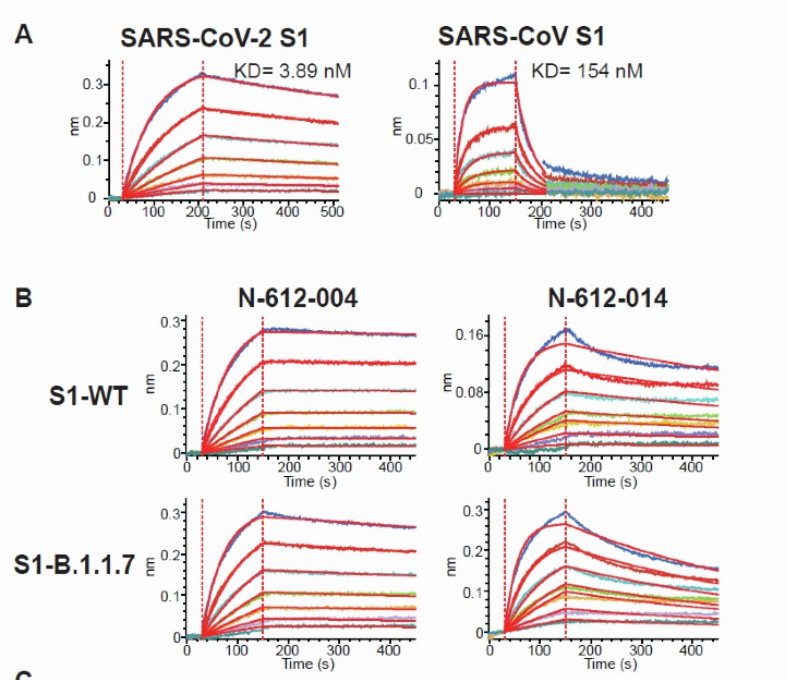

	N-612-004			N-612-014		
nAb	kon (1/Ms)	koff (1/s)	KD (nM)	kon (1/Ms)	koff (1/s)	KD (nM)
S1 wild-type	9.92E+04	1.31E-04	1.32	1.40E+05	1.79E-03	12.8
S1 B.1.1.7	1.13E+05	4.78E-04	4.24	1.68E+05	2.48E-03	14.8

Figure S5: Cross-reactivity of N-612-056 against SARS-CoV (related to Figs 1 and 7 and BLI kinetics analysis method). (A) BLI kinetic analysis of SARS-CoV-2 and SARS-CoV S1 domain binding to N-612-056. (B, C) BLI kinetic analysis of N-612-004 and N-612-014 against S1 domain from WT and B.1.1.7 variant of SARS-CoV-2 Spike protein.